The Astrophysical Journal, 891:90 (20pp), 2020 March 1 https://doi.org/10.3847/1538-4357/ab6d70

Pressure Profiles and Mass Estimates Using High-resolution Sunyaev–Zel'dovich Effect Observations of Zwicky 3146 with MUSTANG-2

Charles E. Romero[1,2], Jonathan Sievers[3], Vittorio Ghirardini[4], Simon Dicker[1], Simona Giacintucci[5], Tony Mroczkowski[6], Brian S. Mason[7], Craig Sarazin[8], Mark Devlin[1], Massimo Gaspari[9,13], Nicholas Battaglia[10], Matthew Hilton[11], Esra Bulbul[4,12], Ian Lowe[1], and Sara Stanchfield[1]
[1] Department of Physics and Astronomy, University of Pennsylvania, 209 South 33rd Street, Philadelphia, PA 19104, USA; ceromero@sas.upenn.edu
[2] Green Bank Observatory, P.O. Box 2, Green Bank, WV 24944, USA
[3] Department of Physics, McGill University, 3600 University Street, Montreal, QC H3A 2T8, Canada
[4] Harvard-Smithsonian Center for Astrophysics, 60 Garden Street, Cambridge, MA 02138, USA
[5] U.S. Naval Research Laboratory, 4555 Overlook Avenue SW, Washington, DC 20375, USA
[6] ESO—European Southern Observatory, Karl-Schwarzschild-Str. 2, D-85748 Garching b. München, Germany
[7] National Radio Astronomy Observatory, 520 Edgemont Road, Charlottesville, VA 22903, USA
[8] Department of Astronomy, University of Virginia, P.O. Box 400325, Charlottesville, VA 22901, USA
[9] Department of Astrophysical Sciences, Princeton University, 4 Ivy Lane, Princeton, NJ 08544, USA
[10] Department of Astronomy, Cornell University, Space Sciences Building, Ithaca, NY 14853, USA
[11] Astrophysics and Cosmology Research Unit, University of KwaZulu-Natal, Westville Campus, Durban 4041, South Africa
[12] Max-Planck-Institute für extraterrestrische Physik (MPE), Gießenbachstraße 1, D-85748 Garching b. München, Germany
Received 2019 August 24; revised 2020 January 7; accepted 2020 January 17; published 2020 March 6

Abstract

The galaxy cluster Zwicky 3146 is a sloshing cool core cluster at $z = 0.291$ that in X-ray imaging does not appear to exhibit significant pressure substructure in the intracluster medium (ICM). The published M_{500} values range between $3.88^{+0.62}_{-0.58}$ to $(22.50 \pm 7.58) \times 10^{14}\,M_{\odot}$, where ICM-based estimates with reported errors <20% suggest that we should expect to find a mass between $6.53^{+0.44}_{-0.44} \times 10^{14}\,M_{\odot}$ (from Planck, with an 8.4σ detection) and $8.52^{+1.77}_{-1.47} \times 10^{14}\,M_{\odot}$ (from ACT, with a 14σ detection). We investigate the ability to estimate the mass of Zwicky 3146 via the Sunyaev–Zel'dovich (SZ) effect with data taken at 90 GHz by MUSTANG-2 to a noise level better than 15 μK at the center and a cluster detection of 61σ. We derive a pressure profile from our SZ data, which is in excellent agreement with that derived from X-ray data. From our SZ-derived pressure profiles, we infer M_{500} and M_{2500} via three methods—*Y–M* scaling relations, the virial theorem, and hydrostatic equilibrium (HE)—where we employ X-ray constraints from *XMM-Newton* on the electron density profile when assuming HE. Depending on the model and estimation method, our M_{500} estimates range from 6.13 ± 0.69 to $(10.6 \pm 2.0) \times 10^{14}\,M_{\odot}$, where our estimate from HE is $7.69^{+2.19}_{-1.98}$ ($\pm$27% stat) $^{+0.63}_{-0.59}$ ($\pm$7.9% sys, calibration) $\times 10^{14}\,M_{\odot}$. Our fiducial mass, derived from a *Y–M* relation is $8.06^{+0.67}_{-0.61}$ ($\pm$7.9% stat) $^{+0.45}_{-0.42}$ ($\pm$5.4% sys, *Y–M*) $^{+0.58}_{-0.54}$ ($\pm$6.9% sys, cal.) $\times 10^{14}\,M_{\odot}$.

Unified Astronomy Thesaurus concepts: Galaxy clusters (584); Intracluster medium (858); Rich galaxy clusters (2005)

1. Introduction

The spatial density of galaxy clusters as a function of mass and redshift can be used to constrain cosmological models (see Allen et al. 2011 and Pratt et al. 2019 for reviews). However, the strength of these cosmological constraints is predominantly limited by the ability to accurately and precisely estimate masses (e.g., Salvati et al. 2018). For galaxy cluster surveys using the Sunyaev–Zel'dovich (SZ) effect (Sunyaev & Zel'dovich 1970, 1972; see Mroczkowski et al. 2019 for a recent review), mass estimates largely come from the *Y–M* scaling relation (e.g., Planck Collaboration et al. 2014; Bleem et al. 2015; Hilton et al. 2018), where *Y* is the integrated SZ signal. The precision of mass estimates from the *Y–M* scaling relation suffer from the intrinsic scatter within these relations (e.g., Sifón et al. 2013; Salvati et al. 2018), while the accuracy can suffer from systematic uncertainties and measurement biases—especially those in the data sample used to establish the scaling relation.

It is convenient to parameterize the strength of the thermal SZ effect in terms of the Compton *y* parameter, which is proportional to the thermal electron pressure integrated along the line of sight, ℓ:

$$y = \frac{\sigma_{\rm T}}{m_e c^2} \int_0^{\infty} P_e\, d\ell, \tag{1}$$

where $\sigma_{\rm T}$ is the Thomson cross section, m_e is the electron mass, c is the speed of light, and P_e is the thermal electron pressure. The integrated *Y* is thus a volumetric integral of the thermal electron pressure, usually computed within a cylinder or a sphere (e.g., Motl et al. 2005; Mroczkowski et al. 2009; Arnaud et al. 2010). We expect that when the gas is fully virialized its energy content is dominated, and thus approximated, as thermal energy. In this case, the thermal energy is directly related to gravitational potential energy (Kaiser 1986; Mroczkowski 2011), and thus there is a direct relation between *Y* and *M*. Even in relaxed, virialized systems, we expect some non-thermal energy and hence some non-thermal energy support (e.g., Shi et al. 2015; Biffi et al. 2016). So long as any non-thermal pressure support (non-thermal kinetic energy) evolves in a self-similar manner (e.g., Nelson et al. 2014b; Yu et al. 2015), an unbroken power-law relation for *Y–M* will hold.

[13] Lyman Spitzer Jr. Fellow.

From SZ observations, there are three common methods of estimating the mass of a cluster: one employs a scaling relation, another employs hydrostatic equilibrium (HE), and the third employs the virial theorem (VT). Masses derived using HE or VT generally omit non-thermal pressure support, and at least for HE, they will consequently be biased low with respect to the total mass (e.g., Miyatake et al. 2019, and references therein). The omission of non-thermal pressure support has generally been forced due to lack of access to this quantity. However, novel approaches such as pressure fluctuation analyses (Khatri & Gaspari 2016), use of high-resolution X-ray spectrometers (Lau et al. 2017), and use of prior knowledge of gas fractions (Eckert et al. 2019) appear to be viable routes to observationally quantifying non-thermal pressure support.

In this paper, we analyze recently obtained deep, high-resolution SZ data on a relatively nearby ($z = 0.291$, Allen et al. 1992), relaxed, massive galaxy cluster, Zwicky 3146.

Being a relaxed cluster of fairly circular shape on the sky means that assuming spherical symmetry should be sufficient, and thus it is an apt cluster to investigate the suitability of the above three mass estimates. A newly developed data processing method allows credible constraints on the pressure profile beyond our (radial) field of view (FOV) and thereby has enabled us to constrain M_{500} with MUSTANG-2 data alone. In addition to fitting pressure profiles, we quantify the residual signal after subtracting point sources and a spherical cluster model.

The layout of this paper is as follows. In Section 2, we discuss the cluster we targeted for observations. In Section 3 we discuss observations with MUSTANG-2 and review the data processing pipelines. In Section 4 we present our map-fitting procedures. In Section 5 we present our results for the pressure profiles and mass estimates, noting deviations from expected results. We discuss our results and potential explanations for them, largely focusing on best methods for mass estimation from SZ data in Section 6 and conclude in Section 7.

Throughout this paper, we adopt a concordance cosmology: $H_0 = 70\,\mathrm{km\,s^{-1}\,Mpc^{-1}}$, $\Omega_M = 0.3$, $\Omega_\Lambda = 0.7$. We define $h_{70} \equiv H_0\ (70\ \mathrm{km\,s^{-1}\,Mpc^{-1}})^{-1}$ and $h(z) \equiv H(z)H_0^{-1}$. At $z = 0.291$, one arcsecond corresponds to 4.36 kpc. Uncertainties assume Gaussian distribution when presented with $\pm$ format, or when values are expressed as M^{+U}_{-L}, M is the median, and U and L express the difference from the median to reach the 16th and 84th percentiles. We report literature values in the latter format, even if the original work provides results in the former format. For results from this work, if multiple uncertainties are presented, the first set is statistical and the last is systematic due to flux calibration; if a third (middle) set is presented, this is the systematic error due to the Y–M relation.

2. The Case of Zwicky 3146

Zwicky 3146 is cross-listed under several names, including ACT-CL J1023.6+0411, BLOX J1023.6+0411.1, PSZ2 G239.43+47.95, RXC J1023.6+0411, and ZwCl 1021.0 +0426. Despite being in the Zwicky catalog (Zwicky et al. 1961), Zwicky 3146 appears to have gone largely unscrutinized until Allen et al. (1992), when it was detected in the *ROSAT* All Sky Survey and followed up through optical spectroscopy from the Faint Object Spectrograph on the Isaac Newton Telescope. Allen et al. (1992) found the Brightest Central Galaxy (BCG) in Zwicky 3146 to be the most line-luminous in their sample. While line emission is common in cooling flow clusters, the observed line luminosities in Zwicky 3146 were found to be well above that expected from recombination of cooling intergalactic medium (IGM; Johnstone et al. 1987). Edge et al. (1994) estimate a pure cooling flow rate of 1250 $M_\odot\,\mathrm{yr^{-1}}$. Subsequent reported rates vary between 300 and 1600 $M_\odot\,\mathrm{yr^{-1}}$ (Egami et al. 2006a; Kausch et al. 2007; McDonald et al. 2018), which is on the upper end of the distribution of pure cooling flow rates. However, such theoretical rates are expected to be quenched down to 10% via active galactic nucleus (AGN) feedback (e.g., Gaspari et al. 2013). We may thus expect greater variability in the core due to feedback processes.

Zwicky 3146 is also remarkable for its H_2 mass, both in a cool and warm state (Egami et al. 2006b). However, in the radio and hard X-rays, Zwicky 3146 is not marked by superlatives (Cooray et al. 1998; Nevalainen et al. 2004). Faint Images of the Radio Sky at Twenty cm (FIRST; White et al. 1997) reveals a 2 mJy central radio source at 1.4 GHz (see Table 7). Giacintucci et al. (2014) used very large array (VLA) data at 4.9 and 8.5 GHz to image the center of Zwicky 3146, finding two sources at each frequency, but only 4.9 GHz shows a radio minihalo. Kale et al. (2015) extended this radio analysis, adding of 610 MHz GMRT data. At 610 MHz, the minihalo shows the same extent and is roughly seven times brighter than at 4.9 GHz, implying a spectral index of $\alpha \sim 0.9$, which is slightly shallower than typical minihalo spectral indices ($\alpha \sim 1.2$–1.3, as reported in Giacintucci et al. 2014).

Simply stated, the interesting part of Zwicky 3146 appears to be its core, where the strong cooling flow and radio minihalo are of particular interest. There is some expectation that, in galaxy clusters in general, these two features will have some correlation (McNamara & Nulsen 2007; Bravi et al. 2016). Forman et al. (2002) identify three edges (or fronts) in *Chandra* data within the central 30″, which they propose may be due to sloshing. Averaged over the entire cluster, Hashimoto et al. (2007) find a minor/major axis ratio of 0.85 using data from the *Chandra* archive. Weißmann et al. (2013) define Zwicky 3146 as being a "regular" cluster, which they define by the lack of substructure in two different Gaussian smoothing kernels ($\sigma = 4''$ and $8''$). Given that $\sigma = 4''$ corresponds closely to the MUSTANG-2 resolution, we should expect minimal substructure in our maps.

The first mass estimate for Zwicky 3146 that we are aware of comes from X-ray studies (Ettori & Fabian 1999; Rasia et al. 2004) and is followed shortly thereafter by an SZ study (McCarthy et al. 2003). When deriving masses from the intracluster medium (ICM), nearly all studies have used a spherical beta (β) model (Cavaliere & Fusco-Femiano 1978) to fit the gas density profile. Often an additional assumption (if only for simplicity or lack of constraint) is that the ICM is isothermal. While this is sufficient to calculate a mass under HE, many papers have added the constraint that the total mass profile be fit by a Navarro–Frenk–White (NFW) (Navarro et al. 1997) profile:

$$\rho(r) = \frac{\rho_0}{(r/R_s)(1 + r/R_s)^2}, \tag{2}$$

where ρ_0 and R_s are the matter density normalization and scaling radius, respectively. Weak-lensing studies have calculated surface mass profiles from shear and subsequently fit those profiles to a NFW profile. It is striking that for the same,

Table 1
Zwicky 3146 Mass Estimates

M_{2500} ($10^{14}M_{\odot}$)	M_{500} ($10^{14}M_{\odot}$)	M_{200} ($10^{14}M_{\odot}$)	Facility	Cosmology Ω_M,$\Omega\Lambda$,h	Estimation Method
⋯	8.13	⋯	*ROSAT* (1, 2)	0.3, 0.7, 0.75	HE, isothermal β and NFW
4.5	10.8	⋯	SuZIE (3)	0.3, 0.7, 1.0	HE, isothermal β and NFW
$3.60^{+1.70}_{-1.70}$	$8.65^{+4.09}_{-4.09}$	$12.3^{+5.8}_{-5.8}$	NOT (4, 5)[a]	0.3, 0.7, 0.7	Shear (WL) and NFW
⋯	$10.81^{+5.90}_{-4.64}$	⋯	NOT (6)[a]	0.3, 0.7, 0.7	Shear (WL) and NFW
⋯	$12.07^{+5.27}_{-5.27}$	$18.72^{+8.18}_{-8.18}$	NOT (5, 6)[a]	0.3, 0.7, 0.7	Shear (WL) and NFW
$5.41^{+0.81}_{-0.81}$	$22.50^{+7.58}_{-7.58}$	⋯	*CXO* (7)	0.3, 0.7, 0.7	HE, β and RTM
⋯	20.8[b]	$28.1^{+\infty}_{-16.3}$	*CXO* (8, 9)	0.3, 0.7, 0.7	HE β and NFW
⋯	5.2[b]	$7.0^{+6.3}_{-2.3}$ $^{+1.2}_{-0.6}$[c]	WFI(10)	0.3, 0.7, 0.7	Shear (WL) and NFW
⋯	7.2[b]	$9.7^{+16.3}_{-6.0}$	*XMM* (10)	0.3, 0.7, 0.7	HE β and NFW
$6.0^{+1.9}_{-1.6}$	14[b]	⋯	*CXO* (11)	0.3, 0.7, 0.7	HE β and NFW
$3.6^{+0.2}_{-0.2}$	8.5[b]	⋯	*CXO* and OVRO/BIMA (12)	0.3, 0.7, 0.7	HE and isothermal β
$3.3^{+0.5}_{-0.4}$	7.7[b]	⋯	OVRO/BIMA (12)	0.3, 0.7, 0.7	HE and isothermal β
⋯	$9.4^{+1.4}_{-1.4}$	⋯	*XMM* (13)	0.3, 0.7, 0.7	Unknown
⋯	$6.72^{+0.44}_{-0.43}$	$10.11^{+0.81}_{-0.77}$	*XMM* (14)	0.3, 0.7, 0.7	HE and NFW
⋯	$8.29^{+0.43}_{-0.42}$	$13.55^{+1.53}_{-1.42}$	*XMM* (14)	0.3, 0.7, 0.7	HE, double β and NFW
⋯	$7.85^{+0.23}_{-0.23}$	⋯	*CXO* (15)	0.3, 0.7, 0.7	double β and Y_X-M[16]
⋯	3.36[b]	4.54	SDSS (17)	0.3, 0.7, 0.72	$L_{1\ \mathrm{Mpc}}$–r_{200} relation[18]
$2.89^{+0.06}_{-0.06}$	$6.82^{+0.14}_{-0.14}$	⋯	*XMM* (19)	0.3, 0.7, 0.7	HE, modified β and parametrized T
$3.27^{+0.41}_{-0.41}$	$7.83^{+0.96}_{-0.96}$	⋯	*CXO* (19)	0.3, 0.7, 0.7	HE, modified β and parametrized T
⋯	7.1	⋯	*CXO* (20)	0.3, 0.7, 0.7	HE β and NFW
⋯	$6.53^{+0.44}_{-0.44}$	⋯	Planck (21)	0.3, 0.7, 0.7	UPP, Y–M[22]
⋯	8.12	⋯	*ROSAT*, *Chandra* (13, 23)	0.272, 0.728, 0.704	T_X–M[24]
$1.69^{+0.34}_{-0.37}$	$3.88^{+0.62}_{-0.58}$	$5.45^{+1.10}_{-0.98}$	Subaru (25)	0.3, 0.7, ?	Shear (WL and NFW)
⋯	$8.53^{+1.77}_{-1.47}$	⋯	ACTPol (26)	0.3, 0.7, 0.7	UPP, Y–M
⋯	$8.28^{+1.19}_{-1.20}$	$12.38^{+1.78}_{-1.79}$	WFI, Subaru (27, 28)	0.3, 0.7, 0.7	Shear

Notes. The facility column refers to the primary instrument(s) used to derive the respective mass. Some masses are not presented (at the tabulated density contrasts) in the original work, but are calculated in another work; in this case we list both references.
[a] NOT is the Nordic Optical Telescope.
[b] If no M_{500} is found in the literature, we use an average conversion from M_{2500} or M_{200} as described in the text. The quoted error bars (except [c]) are from as reported in the literature and vary with respect to the inclusion of systematic uncertainties. NFW refers to the Navarro et al. (1997) profile; RTM refers to the Rasia et al. (2004) profile; UPP refers to the Universal Pressure Profile (Arnaud et al. 2010).
[c] The additional uncertainty ($^{+1.2}_{-0.6}$) reflects best-fit values under different galaxy selections.
References. (1) Ettori & Fabian (1999), (2) McCarthy et al. (2003), (3) Benson et al. (2004), (4) Dahle (2006), (5) Sereno (2015), (6) Pedersen & Dahle (2007), (7) Morandi et al. (2007), (8) Schmidt & Allen (2007), (9) Groener et al. (2016), (10) Kausch et al. (2007), (11) Allen et al. (2008), (12) Bonamente et al. (2008), (13) Mantz et al. (2010), (14) Ettori et al. (2011), (15) Lancaster et al. (2011), (16) Vikhlinin et al. (2009), (17) Wen & Han (2013), (18) Wen et al. (2012), (19) Martino et al. (2014), (20) Walker et al. (2014), (21) Planck Collaboration et al. (2016), (22) Planck Collaboration et al. (2014), (23) Bender et al. (2016), (24) Vikhlinin et al. (2006), (25) Okabe & Smith (2016), (26) Hilton et al. (2018), (27) Nagarajan et al. (2019), (28) Klein et al. (2019).

or ostensibly very similar, assumptions, and especially use of the same data set, the mass estimates vary by almost an order of magnitude; see Table 1.

M_{Δ} is defined as the mass enclosed within a sphere of radius R_{Δ}, and the average (total) matter density is $\Delta\rho_c$, where ρ_c is the critical density of the universe. Common density contrasts in the literature are 2500, 500, and 200. For Zwicky 3146, not all masses in the literature are provided for M_{500}. In this case, we adopt an average conversion from M_{2500} or M_{200}. It is generally found that $0.6 < R_{500}/R_{200} < 0.7$, and that $R_{500}/R_{200} \approx 0.66$ (e.g., Shimizu et al. 2003; Shaw et al. 2008; Battaglia et al. 2012). If we take $\xi = R_{500}/R_{200}$, then $M_{500}/M_{200} = (\xi)^3 * 500/200 = 0.74$ for $\xi = 2/3$. As in Arnaud et al. (2005), we use $R_{2500} = 0.44R_{500}$, or $M_{500} = 2.35M_{2500}$. In Table 1, we do not estimate errors bars for these extrapolated values.

Calculating an expected value from the literature is non-trivial, given that the data sets are not all independent (many make use of the same underlying data) and systematic errors are often not reported. We expect that our MUSTANG-2 derived mass should agree more strongly with other ICM-based masses (i.e., those derived from X-ray or SZ observations). Of the ICM-based masses with reported errors, which are <20%, the highest estimate is $8.52^{+1.77}_{-1.47} \times 10^{14}\ M_{\odot}$ and the lowest estimate (even without the uncertainty criterion) is $6.53^{+0.44}_{-0.44} \times 10^{14}\ M_{\odot}$.

The mass estimates (in units of $10^{14}\ M_{\odot}$) not based on the ICM span from $3.88^{+0.66}_{-0.58}$ to $12.07^{+5.27}_{-5.27}$. Restricting the estimates to only those with reported error bars <20%, we arrive at only one estimate: $3.88^{+0.66}_{-0.58}$, from weak lensing (Okabe & Smith 2016). The tension between this estimate and the lowest one from the ICM (that from Planck) is at 3.3σ.

For reference, with our adopted cosmology at $z = 0.291$, $M_{500} = 8 \times 10^{14}\ M_{\odot}$ corresponds to $R_{500} = 1280$ kpc or $293''$ and $M_{2500} = 3.5 \times 10^{14}\ M_{\odot}$ corresponds to $R_{2500} = 567$ kpc or $130''$.

3. Observations and Data Reduction

3.1. XMM Observations

We analyze the *XMM-Newton* observations of Zwicky 3146 with OBSID 0605540201, 0605540301, and 0108670101, which have 104, 52, and 41 ks of clean MOS2 data, respectively, using the XMMSAS v17.0 software. The processing methodology is as presented in Ghirardini et al. (2018, 2019); we review the methodology below. We extract the spectra of regions with radial edges increasing logarithmically, with minimum width of 0.′5, around the cluster centroids using the XMM-ESAS tools `mos-spectra` and `pn-spectra`, available through the *XMM-Newton* Extended Source Analysis Software (ESAS; Snowden et al. 2008). Point sources detected using the XMM-SAS tool `ewavelet` are masked. We model the source using an absorbed thermal Astrophysical Plasma Emission Code (APEC; Smith et al. 2001; Foster et al. 2012) model with free normalization, metal abundance, and temperature. We jointly analyze data from the same cluster-centric annuli on the sky across all *XMM-Newton* observations. We consider the point-spread function of *XMM-Newton* by computing the crosstalk between all our annuli, thus fitting jointly (simultaneously) all of the spectra, making use of the extended C-statistics (Cash 1979) within the fitting software `Xspec` v12.10 (Arnaud 1996). For the fits, the abundance table is set to the solar measurement reported in Asplund et al. (2009). We exclude from the fit the energy band, where there are bright and time-variable fluorescence lines, as well as the energy band below 0.5 keV where *XMM-Newton* calibration is uncertain. The upper energy cutoffs are those inherent to the MOS and pn instruments: 11.5 keV and 13 keV, respectively.

From the normalization of the APEC model, we can directly get the density, as $K_{\rm APEC} \propto \int n_e^2 dl$. To do so, we employ the onion peeling technique (Ettori et al. 2010), which does not require the assumption of a particular model for the density. To obtain the three-dimensional temperature, we follow the recipe given by Mazzotta et al. (2004), who derived from simulation that the spectral temperature is $T_{\rm sl} = \int W T_{\rm 3D} dV$, where $W = T^{-0.75} n_e^2 \big/ \int T^{-0.75} n_e^2 dV$. Our pressure profile is simply the product of these density and temperature profiles, and has consequently been derived non-parametrically.

3.2. MUSTANG-2 Observations

MUSTANG-2 is a 215 element array of feedhorn-coupled TES bolometers (Dicker et al. 2014). Observing at 90 GHz on the 100 meter Robert C. Byrd Green Bank Telescope (GBT), MUSTANG-2 achieves a resolution of 10″ and has an instantaneous FOV of 4.′25. MUSTANG-2 is the successor to the MUSTANG instrument (Dicker et al. 2008), which had 64 detectors with the same resolution (determined by the telescope optics and coupling), but with only a 42″ FOV. The increased FOV of MUSTANG-2 enables us to recover cluster-sized scales required for the work presented here.

Our observational techniques and data reduction are largely the same as with MUSTANG (see Romero et al. 2015, 2017). We briefly review them here. Absolute flux calibrations are preferentially based on the solar system objects Mars, Uranus, Jupiter, Saturn, and Ceres. We additionally use Atacama Large Millimeter/Submillimeter Array (ALMA) grid calibrators (Fomalont et al. 2014; van Kempen et al. 2014), where the latest observations can be accessed through https://almascience.eso.org/sc/. At least one of the above flux calibrators was observed once per night. To track the telescope pointing and gain, we observe a point source every 30–50 minutes. For Zwicky 3146, we adopt a conservative flux calibration uncertainty of 10%.

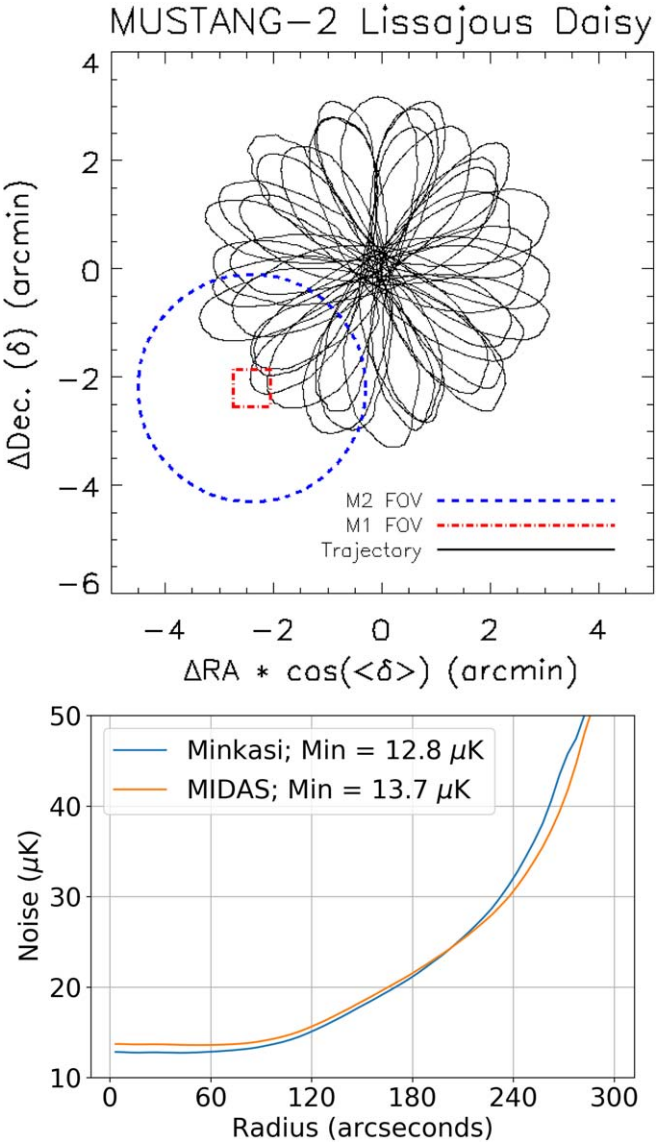

Figure 1. Top: example scan pattern for MUSTANG-2 (M2), which uses the same scan strategy as MUSTANG (M1), scanning at 0.′6 per second, on average. The FOV of the two instruments is plotted for comparison. Bottom: noise (rms) profiles from the two pipelines. Of note is that the profile is relatively flat in the inner 2′.

To observe the target galaxy cluster, we employ Lissajous daisy scans, typically with a 3′ radius (see Figure 1). In the first observing session on Zwicky 3146, we tested scan radii of 2.′5, 3′, and 3.′5 and found that a 3′ radius gave the best mapping speed. Our larger scans employ faster scan speeds, which are generally preferred as it shifts the sky signal to higher frequencies, beyond the $1/f$ noise of the atmosphere or readout. However, to ensure proper pointing, the jerk (third derivative of position, $\dddot{x}$) of the GBT places limits on our scan speed, given the scan pattern. Each of the three scan patterns give a roughly uniform coverage in the central ∼2′. Zwicky 3146 was observed under project ID AGBT18A_175 on the nights of 2018 February 1, 2018 March 18, 2018 March 24, 2018 March 31, 2018 December 12, 2018 December 28, and 2019 January

11, with a total on-source integration time of 22.7 hr. Excising bad scans, our final maps incorporate 21.4 hr of data and have a rms noise of 15 μK (when smoothed to beam resolution) within the central 2′ radius; a more detailed rms profile is shown in Figure 1.

3.3. MUSTANG-2 Data Reduction

We have developed two methods for the processing of MUSTANG-2 data. The first method, called the MUSTANG IDL Data Analysis System (MIDAS), builds off the custom IDL pipeline used with MUSTANG (Romero et al. 2015; Mason et al. 2019); the second method is a maximum likelihood approach (Minkasi). Both techniques include the same initial quality checks (within IDL) performed on the raw data, which we refer to as time ordered data (TOD) from each of the responsive detectors. This paper focuses on the results obtained through the Minkasi pipeline. A comparison of the performance between the two approaches is in Appendix C; here we offer a summary distinction between the two pipelines.

The primary product produced from MIDAS is a (2D) map, where the TODs have been filtered to subtract atmospheric and electronic signal, thus leaving the sky signal. The methods employed to do this subtract some sky signal as well, acting as a high-pass filter and limiting the scales recovered to those within the FOV. In contrast, Minkasi is based on fitting a sky model to the TODs. This sky model can be a map, or for this work, a set of concentric annuli. In both cases, Minkasi does not impose a high-pass filter as MIDAS does. In other words, we can recover scales beyond our FOV. With respect to the concentric annuli, another advantage is that we recover a complete covariance matrix for the annuli, whereas we would need to estimate the covariance matrices for our maps, either in MIDAS or Minkasi.

3.3.1. Minkasi Pipeline

The initial steps of preparing data for processing through Minkasi are as follows: (1) A pixel mask is defined based on the responsivity of the detectors from the instrument setup at the beginning of the run; unresponsive detectors are masked out. (2) Gain and opacity corrections are applied to our data. (3) A noise template is constructed as the common mode across all detectors. This template and a high ($\sim$20) order polynomial are simultaneously fit to and subtracted from the TODs. (4) The cleaned TODs are checked for glitches and a small portion of the TOD (from just before to just after each glitch) is flagged. Detector weights are assigned based on the rms of the corresponding TOD. (5) Rather than make a map, we save the uncleaned but calibrated TOD (before step 3), along with detector weight information (as calculated at step 4).

From here, these saved TODs are passed to the main Minkasi pipeline. The Minkasi pipeline requires some model be proposed. For mapping, each pixel has a corresponding model TOD. The stack of all pixel model TODs is denoted under canonical notation as $\boldsymbol{A}$. The noise (covariance) ($\boldsymbol{N}$) of our data is modeled in Fourier space. In particular, within the Fourier domain, we perform a singular value decomposition (SVD) across detectors per scan. Our noise model is taken as a smoothed version of the SVD-rotated power spectra. Because the number of pixels (and thus models) is so large, exact solutions cannot be obtained directly. Rather, we use a preconditioned conjugate gradient (PCG) descent to obtain our best-fit maps. We find sufficient convergence with 30 to 60 steps in the PCG (Figure 2). This process within Minkasi can be iterated, whereby the previous map (as a TOD) is subtracted when modeling the noise. The entirety of the (original) data, $\boldsymbol{d}$, is still used when calculating $\boldsymbol{A}\ \boldsymbol{N}^{-1}\ \boldsymbol{d}$.

3.3.2. Surface Brightness Profiles

Given an assumed cluster geometry, we opt to fit a surface brightness profile directly to the MUSTANG-2 timestreams within the Minkasi pipeline. The advantage of this approach (over using the map produced with Minkasi) is that we can explicitly solve for the profile and thus recover an accurate covariance matrix. To do this, our (gridding) matrix, which transforms between map and time space, is the same as before. Rather than fit for individual pixel values, we fit for annuli. The annuli may either assume a constant (uniform) brightness within it, or assume a slope dictated by a previous iteration. A model for each annulus is constructed, convolved with the MUSTANG-2 beam (in map space), and converted to a timestream model. Thus, the resulting fits represent a deconvolved surface brightness profile. In the deconvolved surface brightness profile, we find a peak decrement of $722 \pm 99\ \mu$K, or 2.11×10^{-4} in Compton y. When smoothed by the MUSTANG-2 beam, the peak decrement is $676 \pm 23\ \mu$K, or 1.98×10^{-4} in Compton y.

We have tested the ability to recover a known surface brightness profile from synthetic timestreams (noise plus injected model). We generate noise realizations based on the SVD-rotated power spectra, and add an additional white noise level, such that our effective synthetic noise is comparable to that in the real data. We inject a parametric model that is representative of Zwicky 3146. Over many sets of noise realizations, the recovered profiles are well matched to the input profile, with reduced χ^2 values close to 3. We therefore scale our covariance matrix by 3 within Minkasi. When recovering pressure profiles (Section 4.2) and inferring masses (Section 4.3) from these simulated observations, the resultant masses are within the statistical errors of the input model.

4. Fitting Pressure Profiles

4.1. Compact Source Removal

There are six radio sources identified by FIRST (Becker et al. 1994), which correspond to sources found in the MUSTANG-2 maps. Four of the sources appear as two pairs, which from MUSTANG-2 data alone appear non-point-like. All six of these sources are well modeled as point sources. The centroids and FWHM are found in an initial round of fitting. The amplitudes are then fit simultaneously with the surface brightness profiles (Section 3.2). As discussed in Section 5.3, we do find evidence for two additional point sources. At the redshift of Zwicky 3146, the conversion between the reported MUSTANG-2 flux densities (in Jy) and integrated Compton Y (Mpc^2) is $-0.00086\ h_{70}^{-2/3}$. In the MUSTANG-2 data, the total flux density from all point sources is 3 mJy, which is equivalent to $-2.6 \times 10^{-6} h_{70}^{-2/3}$ Mpc^2, which is less than $\lesssim$2.5% of the total $Y_{\rm sph}(R_{500})$ that we find for this cluster.

4.2. Pressure Profile Fitting

The relation between the projected thermal SZ signal and a pressure profile lies in the Compton y parameter, given by

Equation (1). Using the notation in Carlstrom et al. (2002), the change in temperature of the cosmic microwave background (CMB) due to the tSZ is given by

$$\frac{\Delta T_{\rm CMB}}{T_{\rm CMB}} = f(x)y, \tag{3}$$

where $x = h\nu/k_{\rm B}T_{\rm CMB}$ is the scaled frequency, h is the Planck constant, ν is the frequency, $k_{\rm B}$ is the Boltzmann constant, and $T_{\rm CMB}$ is the temperature of the CMB. The function $f(x)$ then governs the spectral distortion of the CMB. We correct for relativistic corrections; thus $f(x)$ is actually $f(x, T_e)$, as given by Itoh et al. (1998). As $f(x, T_e)$ is only a weak function of temperature for typical cluster temperatures ($k_{\rm B}T_e < 15$ keV) and observations at 90 GHz, we assume $k_{\rm B}\,T_e = 7$ keV, which is within the spread of temperatures reported in the literature (references cited in Table 1). Additionally, our maps are calibrated to brightness temperature (i.e., a Rayleigh–Jeans brightness temperature, $T_{\rm B}$). The conversion comes from the derivative of the Planck function and at 90 GHz, $\Delta\ T_{\rm CMB}/T_{\rm B} = 1.23$ (see, e.g., Finkbeiner et al. 1999; Mroczkowski et al. 2019).

In our non-parametric (NP) pressure profile model, we assume a power-law distribution of pressure within radial bins. We define 12 bins with the 3 innermost bins linearly spaced (10″, 20″, and 30″) and subsequently logarithmically spaced radii out to 5′. The linearly spaced inner bins ensures that they are spaced a beamwidth apart. The innermost bin, being a circular (not annular) aperture, is larger than our beam, offering slightly better constraints than a bin matched to a 10″ FWHM (i.e., 5″ half width, half max [HWHM]).

The slope of the pressure in the innermost bin is determined by a normalization at $r = 5''$ and at $r = 10''$. The outermost bin spans from 225″ to infinity with the slope and normalization determined by the pressure at $r = 225''$ and $r = 300''$. All other bins span between neighboring radii (edges).

We also directly fit the generalized NFW pressure profile (Nagai et al. 2007):

$$P(r) = \frac{P_0 P_{500}}{(C_{500}r/R_{500})^{\gamma}(1 + (C_{500}r/R_{500})^{\alpha})^{(\beta-\alpha)/\gamma}}, \tag{4}$$

where P_0, C_{500}, α, β, and γ were established as free parameters, and

$$P_{500} = 1.45 \times 10^{-11}\left(\frac{M_{500}}{10^{15}h^{-1}M_{\odot}}\right)^{2/3} E(z)^{8/3}, \tag{5}$$

and $E(z)^2 = \Omega_{\rm M}(1+z)^3 + \Omega_{\Lambda}$. As many of the gNFW parameters are degenerate, interpreting physical meaning from the fitted values is more difficult when all parameters are allowed to vary. Thus, we choose to fix α, β, and γ to their respective values found in Arnaud et al. (2010) (hereafter, A10): 1.05, 5.41, and 0.31; we refer to the gNFW profile with these restrictions as an A10 profile. The Compton y profile for the A10 (pressure) profile is computed via numerical integration, with line-of-sight bounds at $\pm 5R_{500}$, for the fiducial $M_{500} = 8 \times 10^{14}\,M_{\odot}$. We find that our mass results are quite independent of the integration constraint (out to $5R_{500}$); they vary by at most 1.1% between adopting a fiducial mass $M_{500} = 16 \times 10^{14}\,M_{\odot}$ and $M_{500} = 4 \times 10^{14}\,M_{\odot}$.

The A10 pressure profile that we adopt here is slightly more general than the universal pressure profile (UPP) presented in A10. That is, for the UPP, C_{500} is fixed, and P_{500} and R_{500} are functions of mass (M_{500}). Even with the normalization and C_{500} allowed to vary, we have constrained the profile shape such that uncertainties on our pressure profile and subsequently derived quantities are artificially small. In Section 6.2, we compare our NP and A10 fitted pressure profiles and discuss the impact on mass estimation in Section 6.3.1.

When fitting to the surface brightness profile found with Minkasi, the Compton y profile is converted to a $T_{\rm B}$ profile and matched to the bin normalizations reported by Minkasi. As Minkasi reports a full covariance matrix associated with the bin normalizations, this is used when determining the likelihood of each model. In both cases, the fitting is done with the MCMC package `emcee` (Foreman-Mackey et al. 2013).

The choice of adopting spherical symmetry is motivated by (1) the ease of interpretation of results and comparison to the literature, and (2) our data suggest that a globally ellipsoidal model is not necessary. In Figure 3, we calculate axis ratios based on isophotes at several radii. While the center exhibits high ellipticity, beyond an arcminute, the cluster isophotes are close to circular. That is, an ellipse that fits the center will not be appropriate for the majority of the cluster-centric radii.

4.3. Mass Derivations

We investigate mass estimates via three avenues: (1) employing a Y–M relation, (2) employing spherical HE, and (3) employing the VT as in Mroczkowski (2011). The first and third methods can be done with SZ data alone, while the second avenue requires knowledge of the gas density (or electron density), obtained here from analysis of *XMM-Newton* data.

The uncertainty on our flux calibration (Section 3.2) leads to a systematic uncertainty in our derived pressure profiles and consequently in each of our mass estimations. Thus, we calculate an uncertainty in our mass estimation by propagating this flux calibration uncertainty.

4.3.1. *Via* Y–M *Relation*

There are two flavors of integrated Y quantities: $Y_{\rm cyl} = Y_{\rm SZ}D_{\rm A}^2$ (A10) and $Y_{\rm sph}$. The two are calculated as follows:

$$Y_{\rm SZ}(\theta) = \frac{\sigma_{\rm T}}{m_e c^2}\int_0^{\theta}\left[\int_{-5R_{500}}^{5R_{500}} P_e(\ell)\,d\ell\right]2\pi\theta\,d\theta \tag{6}$$

$$Y_{\rm sph}(R) = \frac{\sigma_{\rm T}}{m_e c^2}\int_0^{R} 4\pi P_e(r)\,r^2\,dr, \tag{7}$$

where r is the physical radius, θ is the angular (projected) radius, and for $Y_{\rm cyl}$, ℓ is the distance along the line of sight. $Y_{\rm cyl}$ is often reported in units of Mpc^2, rather than steradians. We opt to use the $Y_{\rm sph}$ relation, as it is easily integrated analytically.

As a Y–M relation only applies to a specific radius, we adopt Y–M relations at R_{500} and R_{2500}; at each radius, we calculate the mass via three different relations. At R_{500}, we adopt the relations in A10, Marrone et al. (2012, hereafter M12), and Planelles et al. (2017, hereafter P17). At R_{2500}, we adopt the relations in Comis et al. (2011, hereafter C11), M12 and P17. At each step in the MCMC pressure profile fits, we compute $Y_{\rm sph}(R)$ and derive a self-consistent R_{500} (see Appendix A) for each Y–M relation. Systematic uncertainties on Y–M are calculated using the uncertainties on the Y–M parameters

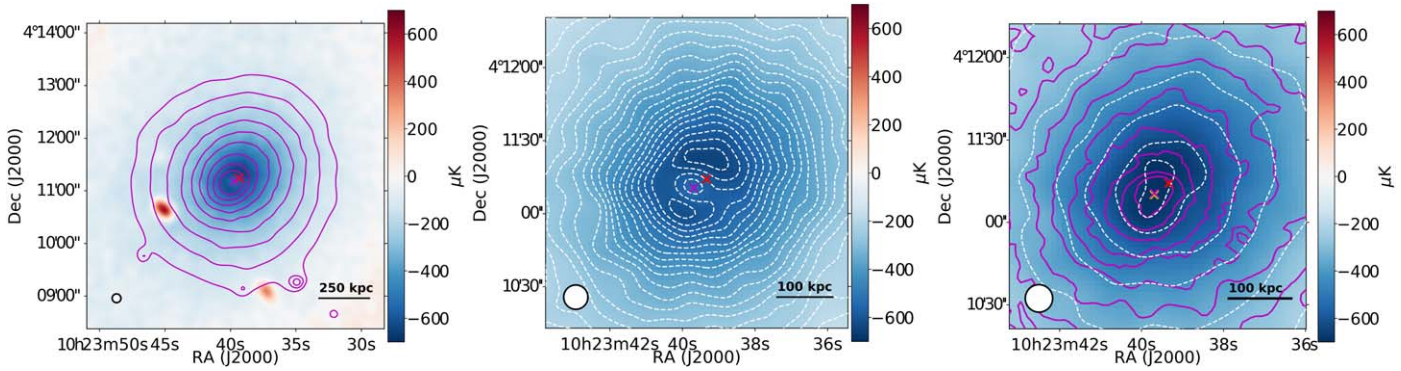

Figure 2. MUSTANG-2 images of Zw 3146. Left: Minkasi map, zoomed out, with smoothed X-ray surface brightness contours from *XMM* in magenta. Middle: Minkasi map, zoomed in, with significance contours (every 2σ) in white. Right: point-source subtracted Minkasi map (Section 4.2) with contours (white) at $[-54, -50, -42, -34, -26, -18]\sigma$ and X-ray (*Chandra*) surface brightness contours overlaid in magenta. The red cross denotes the SZ centroid; the magenta cross denotes the X-ray (*XMM*) centroid.

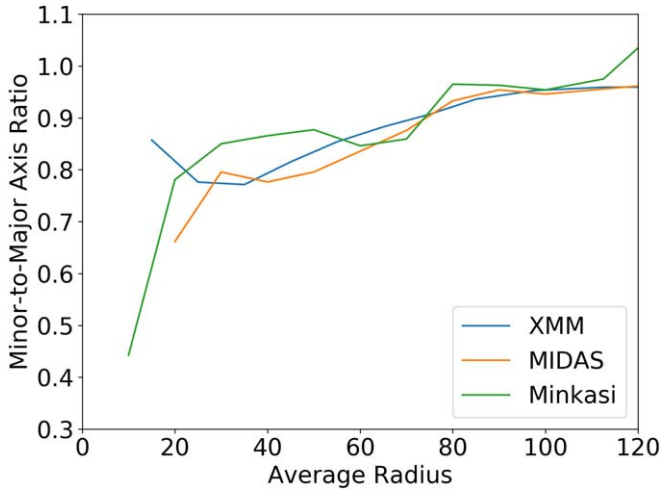

Figure 3. Minor-to-major axis ratios (for axes in the plane of the sky) as determined via our two map-making procedures, with a comparison to the X-ray (*XMM-Newton*) image.

reported the respective paper. If covariances are listed, they are used; otherwise, the uncertainties are assumed to be independent.

4.3.2. Via Hydrostatic Equilibrium

Under HE, pressure and gravity are related by

$$\nabla P = -\rho_g \nabla \phi, \tag{8}$$

where P is the total gas pressure, ρ_g is the gas-mass density, and ϕ is the gravitational potential (see, e.g., Sarazin 1988). If we assume a spherically symmetric, non-rotating ICM with homogeneous metallicity and electron–ion equipartition, we can rewrite this as

$$\frac{dP_e}{dr} = -\mu m_p n_e G \frac{M_{\rm HE}(<r)}{r^2}, \tag{9}$$

where μ is the mean molecular weight, m_p is the proton mass, n_e is the electron (count) density, G is the gravitational constant, and $M_{\rm HE}$ is the total (dark matter + baryonic) mass enclosed within radius r. We adopt $\mu = 0.61$ (e.g., Eckert et al. 2019).

In practice, we rewrite Equation (9) as follows:

$$M_{\rm HE} = -\frac{d\ln P_e}{d\ln r}\frac{P_e}{n_e}\frac{r}{\mu m_p G}. \tag{10}$$

From SZ data alone, we lack n_e. If we assume a temperature profile (isothermal or, perhaps, a Vikhlinin profile; Vikhlinin et al. 2006, hereafter V06), we can calculate n_e from the SZ-derived P_e. However, a temperature normalization is still necessary. For Zwicky 3146, many temperatures are published in the literature. Given an initial mass (M_{500}) estimate, one could calculate T_X from its scaling relation with M. In this work, we make use of an electron density profile from *XMM* (following Ghirardini et al. 2018). Mass profiles are calculated as a function of radius, and a self-consistent R_{500} is calculated as shown in Appendix A for each step in the MCMC.

4.3.3. Via Virial Equilibrium

One can also assume that the ICM is in virial equilibrium, which derives from statistical mechanics and relates the total kinetic energy, $E_{\rm kin}$ to the gravitational potential energy, U_g:

$$2E_{\rm kin}(R) = -U_g(R). \tag{11}$$

Mroczkowski (2011) take the kinetic energy to be the thermal energy $E_{\rm kin} = E_{\rm th}$, while the erratum considers an external surface pressure term (Mroczkowski 2012; see, e.g., Kippenhahn et al. 2012 for a general discussion). This results in the virial relation in the form: $2E_{\rm th} - 3P(R)V = -U_g(R)$. Here, R is the outer radius of the system and V is the total volume. Assuming an NFW matter profile, they derive an expression, which includes a definite integral. Here, we express this relation with the integral solved:

$$\frac{\mu_e}{16\pi^2 G\mu f_{\rm gas}}\left[3\frac{m_e c^2}{\sigma_{\rm T}}Y_{\rm sph}(R) - 4\pi R^3 P_e(R)\right] = \rho_0^2 R_s^5\left[\frac{R/R_S - \ln(1+R/R_s)}{1+R/R_S} - \frac{1}{2(1+R_s/R)^2}\right], \tag{12}$$

where μ_e is the electron mean molecular mass (mean molecular mass per electron), $f_{\rm gas}$ is the gas fraction, ρ_0 and R_s are the matter density normalization and scaling radius, respectively, in the NFW profile (Equation (2)). As in Mroczkowski (2011), we take $\mu_e = 1.17$ and $f_{\rm gas} = 0.13$. We note that $\mu_e = 1.17$ is

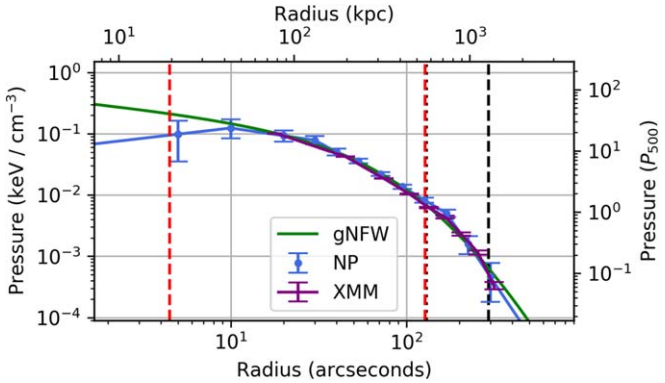

Figure 4. Two fitted pressure profile models for Zwicky 3146, as well as the pressure profile as determined from *XMM-Newton*. The vertical red dashed lines are the HWHM and radial FOV for MUSTANG-2; the vertical black dashed line is R_{500} for $M_{500} = 8 \times 10^{14} M_{\odot}$ and the vertical black dotted line (just to the right of the right red dashed line) is R_{2500} for $M_{2500} = 3.5 \times 10^{14} M_{\odot}$.

consistent with $\mu = 0.61$ (Eckert et al. 2019). Because this approach requires fitting the left-hand side of Equation (12) to its right-hand side, we do this at the end of the MCMC to use appropriate error bars. We exclude the points within the central 100 kpc, as is often done in X-ray analyses in cool core clusters; additionally, as discussed in Section 5, our constraints in the central 100 kpc are prone to degeneracies with the central point sources. Error bars on the NFW parameters ρ_0 and $1/R_s$ are computed within the least square fitting algorithm scipy.opt. curve. Subsequently, M_{500} is calculated self-consistently from the NFW mass curve (as for the hydrostatic mass) over 1000 iterations with the covariance matrix on ρ_0 and $1/R_s$, as returned by the fitting routine. The parameters ρ_0 and $1/R_s$ are fit rather than ρ_0 and R_s, as the former pair have a roughly linear covariance.

5. Results

5.1. Pressure Profiles

We expect our best pressure profile constraints over radial scales ranging from the HWHM of the beam out to the radial FOV (i.e., from 5 to 126″ for MUSTANG-2), where the constraints beyond the (radial) FOV are often quite limited for ground-based single dish SZ instruments (e.g., Adam et al. 2014; Czakon et al. 2015; Romero et al. 2018; Ruppin et al. 2018; Sayers et al. 2019; Di Mascolo et al. 2019). Moreover, we may expect the tightest constraints around the geometric mean of the HWHM and radial FOV (Romero et al. 2015). As seen in Figure 4, MUSTANG-2 produces tight constraints (<25%) between $30'' < r < 200''$, with the tightest fractional constraint occurring in our bin just beyond 1′. The constraints in the center ($r < 30''$) are poor owing to the presence of two known radio sources, one of which was fit for, while the other we investigate in Section 5.3. Ellipticity and low-level substructure might be responsible for the difference in the pressure of the central most bin in the NP model as compared to the gNFW model. We find that centroid choice (between the X-ray or SZ centroid) has a negligible impact on the pressure profile.

5.2. Mass Estimates

For each pressure profile we fit, we estimate the cluster mass via the three methods presented in Section 4.3; our M_{500} and M_{2500} estimates are shown in Table 2. We find that at R_{500}, $M_{\rm VT}$ yields the largest mass estimates for each pressure profile and $(Y\text{–}M)_{\rm A10}$ to be the smallest mass estimates. The best-fit NFW parameters for the NP pressure profile are $\rho_0 = 24 \pm 5\ {\rm g\,cm^{-3}}$ and $R_s = 667 \pm 76$ kpc, and for the gNFW pressure profile, $\rho_0 = 23.2 \pm 0.3\ {\rm g\,cm^{-3}}$ and $R_s = 697 \pm 6$ kpc, where the error bars are once again small owing to our restriction of the gNFW pressure profile shape.

The agreement or disagreement of $M_{\rm HE}$ with the other mass estimates also highlights a key procedural/mathematical difference between the methods of estimation: we calculate $M_{\rm HE}$ at individual radii, which does not make use of knowledge of the pressure profile across all radii. However, the Y–M mass makes use of Y, a cumulative sum of spherically integrated pressure within R_{500} (or R_{2500}). Similarly, $M_{\rm VT}$ is fit across all pressure bins at radii larger than 100 kpc.

Physically, we may expect $M_{\rm HE}$, $M_{\rm VT}$, and $(Y\text{–}M)_{\rm A10}$ (or $(Y\text{–}M)_{\rm C11}$ for M_{2500}) to be similar, as they directly or indirectly rely on the assumption of HE. The other Y–M relations, being calibrated to weak lensing or simulations, should encapsulate the total mass without regard to dynamical state.

We expect mass estimates that assume HE underestimate the total mass due to the so-called hydrostatic mass bias, which itself encompasses several biases. The primary bias is not actually the HE assumption, but rather that the pressure gradient used only accounts for thermal pressure. Thus the lack of account for non-thermal pressure underestimates the mass by 10%–30% (see also Lau et al. 2013; Nelson et al. 2014a; Biffi et al. 2016; Khatri & Gaspari 2016; Hurier & Angulo 2018; Ettori et al. 2019).

5.3. Residuals

An underlying quadrupole is observed in our residual map (Figure 5). Modeling the ICM with the same centroid and an ellipsoidal ICM distribution results in very similar residual decrements and removes this quadrupole. Beyond ellipticity in the core of the cluster, the only observed SZ substructure is also in the core of the cluster. The corresponding integrated Y ($Y_{\rm cyl}$) due to the substructure (decrement $<-25\ \mu$K) is $3.0 \times 10^{-7}\ h_{70}^{2/3}$ Mpc^2, whereas we find $Y_{\rm cyl}(R_{500}) = 7.3 \times 10^{-5} h_{70}^{2/3}$ Mpc^2 for our NP fit; thus substructure accounts for only 0.5% of the SZ signal within θ_{500} and is not a significant source of scatter in the mass estimates from Y–M relations for this cluster.

As noted before, the central pressure profile and the central point-source amplitude are degenerate. In addition to the central radio source, a second, nearby radio point source is observed at 4.9 and 8.5 GHz (Giacintucci et al. 2014). We find that these two sources contribute to a mild increase in the uncertainties in the inner two pressure profile bins.

The spatial coincidence of our residual SZ decrement and the radio minihalo (Figure 6) may be suggestive of an underlying link. It would be equally interesting if there is a link between the SZ residual and the noted sloshing (Forman et al. 2002).

5.4. SZ/X-Ray Products

Given the SZ and X-ray data in hand, we extend our profile analyses to other thermodynamic quantities—namely, temperature and entropy. Given the better performance of Minkasi results (NP

Table 2
MUSTANG-2 Mass Estimates

M_Δ	Model	$(Y–M)_1$ $(10^{14}M_\odot)$	$(Y–M)_2$ $(10^{14}M_\odot)$	$(Y–M)_3$ $(10^{14}M_\odot)$	$M_{\rm HE}$ $(10^{14}M_\odot)$	$M_{\rm VT}$ $(10^{14}M_\odot)$
M_{500}	NP	$8.06^{+0.67+0.45+0.58}_{-0.61-0.42-0.54}$	$6.41^{+0.37+0.04+0.35}_{-0.36-0.04-0.33}$	$7.69^{+0.70+0.10+0.59}_{-0.64-0.10-0.55}$	$7.69^{+2.19+0.63}_{-1.98-0.59}$	$10.6^{+1.1+0.9}_{-1.1-0.8}$
	gNFW	$7.63^{+0.29+0.41+0.56}_{-0.28-0.39-0.52}$	$6.13^{+0.17+0.19+0.33}_{-0.17-0.19-0.32}$	$7.29^{+0.31+0.09+0.57}_{-0.28-0.09-0.53}$	$7.66^{+0.76+0.91}_{-0.68-0.83}$	$10.6^{+0.1+0.9}_{-0.1-0.8}$
M_{2500}	NP	$3.42^{+0.51+0.79+0.45}_{-0.46-0.64-0.42}$	$3.04^{+0.34+1.28+0.33}_{-0.32-0.90-0.31}$	$2.76^{+0.38+0.06+0.32}_{-0.35-0.06-0.30}$	$3.37^{+0.79+0.74}_{-0.88-0.50}$	$3.53^{+0.19+0.36}_{-0.18-0.33}$
	gNFW	$3.33^{+0.23+0.77+0.43}_{-0.21-0.62-0.40}$	$2.97^{+0.16+1.20+0.31}_{-0.15-0.85-0.29}$	$2.70^{+0.17+0.06+0.31}_{-0.15-0.05-0.29}$	$4.53^{+0.34+0.86}_{-0.31-0.75}$	$3.65^{+0.02+0.37}_{-0.02-0.34}$

Note. Mass estimates from MUSTANG-2 (and electron density profiles from *XMM*) for $M_{\rm HE}$. $M_{\rm VT}$ is not the virial mass, as is classically defined (with respect to $R_{\rm vir}$), but rather the mass within R_Δ using the Virial theorem (Mroczkowski 2011). The error bars on the *Y–M* mass are, in order, the statistical error, systematic error from the *Y–M* relation itself, and the systematic error due to calibration uncertainty. The error bars on the other mass estimates are the statistical and systematic error due to calibration uncertainty. The *Y–M* relations for M_{500} for the subscripts 1, 2, and 3 are A10, M12, P17, respectively; for M_{2500}, the relations come from C11, M12, P17, respectively.

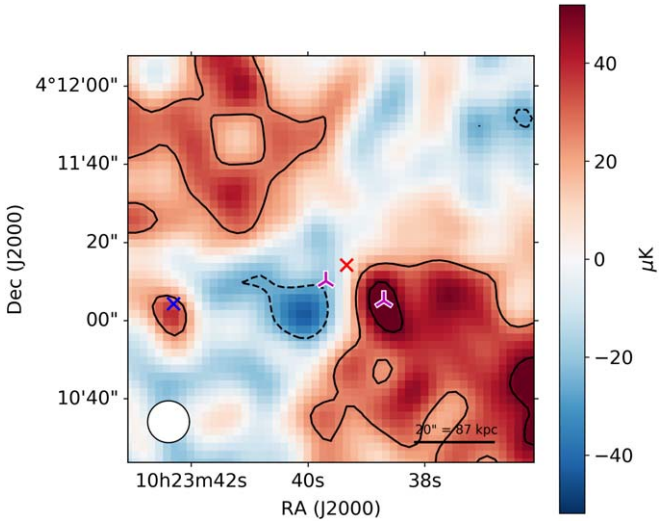

Figure 5. Residual map (in μK) of the Minkasi map with the SZ centroid marked by a red cross, the radio sources marked by tri_up (purple on white), and the Herschel 500 micron centroid by a blue cross; the beam is shown in the bottom left. The black contours are every 2σ, excluding 0 ($\sigma = 12.8$ μK).

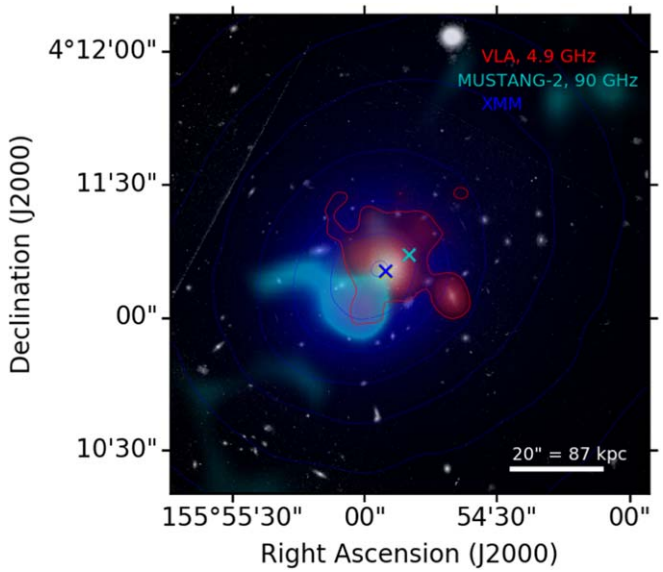

Figure 6. *Hubble Space Telescope* image with MUSTANG-2 residual (cyan), X-ray (*XMM*, blue), and radio (4.5 Ghz, red) overlays. The cyan (blue) cross is the X-ray (SZ) centroid.

and gNFW), we do not include the MIDAS pipeline results in these analyses.

5.4.1. Temperature

We compute our temperature as

$$k_{\rm B}T_e = P_e/n_e, \tag{13}$$

where P_e is determined from our SZ data and n_e comes from X-ray data. We use T in keV as shorthand for $k_{\rm B}T_e$.

In order to assess how our temperature profile compares with others in the literature, we fit our results to two parameterizations from V06 (hereafter, V06). The first (Equation (14)) is a general parameterization, which should accommodate variations of shape between cluster temperature profiles. The second parameterization (Equation (15)) was found as an approximation to the average temperature profile across the cluster sample in V06; it has a fixed shape, with only the normalization being allowed to vary. Therefore, comparison to this second curve gives some indication of how "average" Zwicky 3146 is, with respect to the sample in V06,

$$T(r) = T_0 \frac{(r/r_t)^{-a}}{[1+(r/r_t)^b]^{c/b}} \frac{(r/r_{\rm cool})^{a_{\rm cool}} + T_{\rm min}/T_0}{(r/r_{\rm cool})^{a_{\rm cool}} + 1}, \tag{14}$$

and a simplified form (which approximated an average temperature profile):

$$\frac{T(r)}{T_{\rm mg}} = \frac{(x/0.045)^{1.9} + 0.45}{(x/0.045)^{1.9} + 1} \frac{1.35}{(1+(x/0.6)^2)^{0.45}}, \tag{15}$$

where in Equation (14), all other variables except r are fitted parameters, and in Equation (15), $x = r/r_{500}$ and $T_{\rm mg}$ is the gas-mass-weighted temperature. In the general form, we opt to restrict the parameters $a = 0$ and $b = 2$, as in Ghirardini et al. (2019), and furthermore $c = 3$, where this was found to be a good fit to the gNFW-derived temperature profile. The fitted curves with a, b, and c fixed look very similar to all variables being fit. Fixing these variables helps with variable degeneracies and consequently associated uncertainties. Figure 7 shows our temperature profiles along with these fitted parameterizations; the parameters themselves are listed in Table 3.

We note that Equation (14) has more free parameters than are necessary to fit our temperature profiles. The (approximate) average temperature profile (Equation (15)) does not appear to be as good of a fit. In V06, they find one cluster (A2390),

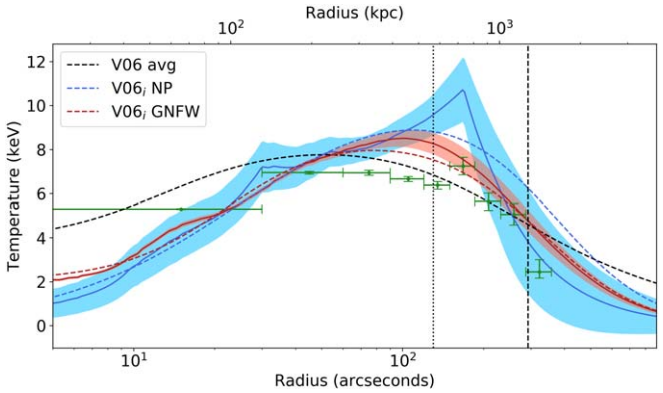

Figure 7. Temperatures as inferred from the SZ (Minkasi pipeline) pressure and the X-ray-derived electron density. The red curve and uncertainty band is from the gNFW pressure profile, and the blue curve is from the NP pressure profile. The green points are spectroscopically derived X-ray temperatures, T_X. The black dashed temperature curve is the approximate average temperature profile found in V06 (their Equation (8)), with $T_{\rm mg}$ fitted. The blue and red dashed curves are the fitted "individual" Vikhlinin profiles (Equation (6) in V06, denoted here as VO6$_i$) as fitted to the SZ temperatures as determined using the NP and GNFW pressure profiles, respectively. The dotted and dashed vertical lines are as in Figure 4.

which has a similar shape as ours; A2390 was noted as having an unusual temperature profile in their sample due to the central AGN in that cluster.

5.4.2. Entropy

Entropy is potentially equally important to pressure or temperature for studying the evolution of clusters. Additionally, as convective stability is achieved when $dK/dr \geqslant 0$, it determines the structure of the ICM (e.g., Voit 2005).

We adopt the entropy parameter K_e (hereafter "entropy") as defined in Voit (2005), where

$$K_e = k_{\rm B} T n_e^{-2/3} = P_e n_e^{-5/3}. \quad (16)$$

From Voit (2005) and references therein, we expect this proxy for entropy to follow as a function of radius a power law $K_e(r) \propto r^{1.1}$, with some deviation at small radii ($r \lesssim 0.1 r_{200}$), where the entropy profiles flatten toward the core. More recent works (e.g., Cavagnolo et al. 2009; Pratt et al. 2010; Ghirardini et al. 2019) continue to find overall agreement with the so-called Voit profile, especially over sample averages. However, some differences, are found. Cavagnolo et al. (2009) found a slightly steeper power-law slope ($\alpha = 1.21 \pm 0.39$) across the entire sample, which is still consistent with the Voit profile. Conversely, Ghirardini et al. (2019) found a slope of $\alpha = 0.84 \pm 0.04$ at large radii.

Our entropy profiles, shown in Figure 8, exhibit some noise in the central region in the NP fit and show a turnover at large radii. We fit the power-law slope over the range $100 < r$ (kpc) < 600 and found $\alpha_{\rm NP} = 1.39 \pm 0.09$ and $\alpha_{\rm gNFW} = 1.40 \pm 0.006$. Note that by restricting the shape of the pressure profile, the gNFW parameterization reduces our uncertainty on the entropy slope. For completeness, if we use all but the last bin in the NP model (i.e., $r < 1000$ kpc), then the fitted slope is $\alpha = 1.47 \pm 0.06$.

5.4.3. Gas Fraction

We expect the matter content of galaxy clusters to be approximately those of the universe. That is, we expect $f_{\rm gas}$ to be close to Ω_b/Ω_m, and measuring this can help us understand how matter is accreted and processed. Measuring $f_{\rm gas}$ is notoriously difficult, certainly in the IGM. However, given the robust constraints on $f_{\rm gas}$, especially from simulations, $f_{\rm gas}$ can be used to gauge clumping (e.g., Simionescu et al. 2011). More recently, when assuming a functional form for the profile of $f_{\rm gas}$, it can be used with the gas-mass profile and the hydrostatic mass profile to quantify the non-thermal pressure support (Eckert et al. 2019).

In particular, we expect that $f_{\rm gas} < \Omega_b/\Omega_m$, largely due to formation processes (e.g., LaRoque et al. 2006) and a small amount of baryons, will also be locked up in stars. Another point of comparison is that Mantz et al. (2016) found an average $f_{\rm gas}(R_{500}) = 0.125 \pm 0.005$, where most of our gas fractions at R_{500} are in agreement with this value, while the gas fraction derived from our $(Y\text{–}M)_{\rm M12}$ masses is in mild tension. Figure 9 shows the gas fractions as calculated with respect to total masses from Y–M relations (upper panel) and from HE (lower panel). The total mass profiles for the Y–M relations fit a NFW mass profile to the respective mass pair of M_{2500} and M_{500} in the NP pressure profile model. Thus the blue curve (A10/C11) in the top panel uses an NFW mass profile fitted to $M_{500} = 8.06^{+0.67}_{-0.61} \times 10^{14} M_\odot$ and $M_{2500} = 3.42^{+0.51}_{-0.46} \times 10^{14} M_\odot$.

6. Discussion

6.1. SZ Substructure

Simulations consistently have shown that pressure, which underlies the Compton y, equilibrates more quickly than other thermodynamic parameters (e.g., Motl et al. 2005; Nagai et al. 2007). The typical timescale for pressure equilibration is characterized by the sound crossing time, which for most massive clusters is ~1 Gyr (e.g., Sarazin 1988, 2003). With no clear evidence of a recent, strong merger, it is not surprising that the residual signal (0.5%) is less than a few percent of $Y_{\rm cyl}(R_{500})$, since by most metrics this is a relaxed, cool core cluster.

By way of comparison, we highlight the case of the well-known, strongly sloshing X-ray luminous cluster RX J1347.5-1145 (Komatsu et al. 2001; Kitayama et al. 2004, 2016; Ueda et al. 2017). RX J1347.5–1145 is a dramatic and likely late-stage merger that is arguably more disturbed than Zw 3146 and has two clear lensing peaks traced by two equally bright "brightest cluster galaxies" (e.g., Ueda et al. 2017). The excess SZ residual reported in Korngut et al. (2011) and Plagge et al. (2013) and attributed to the SE enhancement is only ≈9%–10% of the total SZ signal within R_{500}. However, this estimate comes about when fixing the centroid to the X-ray peak and assuming spherical symmetry, rather than determining the centroid and geometry from the SZ data. As shown in Di Mascolo et al. (2019), an ellipsoidal pressure profile model with a floating centroid fits RX J1347.5-1145 with no significant residuals across a broad range of scales and observations, including the 12 meter ALMA in compact configuration (≈5″ resolution), the 7 meter Atacama Compact Array (≈15″ resolution), Bolocam (≈1′ resolution), and *Planck* (≈10′ resolution). It is therefore unsurprising that Zw 3146 can also be described well by a continuous pressure distribution,

Table 3
Temperature Parameters

Model	T_0 (keV)	r_t (Mpc)	$T_{\rm min}/T_0$	$r_{\rm cool}$ (kpc)	$a_{\rm cool}$
NP	11.2 ± 4.6	1.93 ± 1.01	0 ± 0.41	110 ± 54	1.3 ± 1.0
gNFW	8.8 ± 0.1	1.80 ± 0.02	0.23 ± 0.01	98 ± 2	2.15 ± 0.05
Priors	$U(0, 30)$	$U(0, 5)$	$U(0, 1.0)$	$U(0, 400)$	$U(0, 10)$

Note. Fitted parameters for temperature profiles to Equation (14), fixing $a = 0$, $b = 2$, and $c = 3$. We apply limits to the fitted parameters; these are expressed in the table as adding uniform priors between the lower, l, and upper, u, bounds: $U(l, u)$.

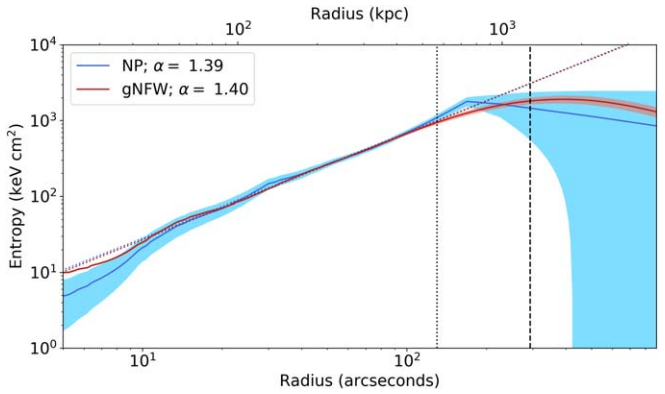

Figure 8. Entropy profile from MUSTANG-2-derived pressure and *XMM*-derived electron density, calculated as in Equation (16). The error bars are solely statistical. The vertical lines are as in Figure 4.

though we note again that in the case of Zw 3146, the centroid choice does not strongly affect the inferred pressure profile (see Section 5.1).

We revisit briefly the ellipticity found in Zwicky 3146. (Kravtsov & Borgani 2012, Section 3.4) remark that isopotential surfaces in equilibrium are more spherical than the underlying mass distribution. Moreover, as baryons flow to the center, the underlying dark matter distribution is expected to be more spherical with decreasing cluster-centric radius (Kravtsov & Borgani 2012, Section 3.5.3, and references therein). In Romero et al. (2017), the tendency for a more spherical core was also noted. Thus the increase in ellipticity toward the center of Zwicky 3146 appears unusual and could be related to the sloshing in the core. A more detailed study of the sloshing scenario in this cluster is in preparation.

6.2. Recovery of Pressure Profile

Several previous ground-based single dish SZ studies have concluded that they cannot constrain the pressure profile of a cluster beyond the instrument's radial FOV (Section 5.1) or, similarly, they have concluded that an attempt to constrain the profile beyond the radial FOV may be biased (e.g., Sayers et al. 2016). Thus, achieving constraints on the pressure profile to better than 25% out to 200″, nearly twice our radial FOV, is a marked improvement.

Our constraints diminish rapidly beyond 240″ for multiple reasons: (1) our coverage drops off rapidly beyond this scale (due to the scanning radius used in mapping; see Figure 1), (2) the cluster SZ signal is weaker, and (3) our surface brightness profile binning will be larger, and thus more susceptible to degeneracy with large-scale ($\gtrsim$FOV) modes from the atmosphere. However, we note that, so long as the low-k modes can

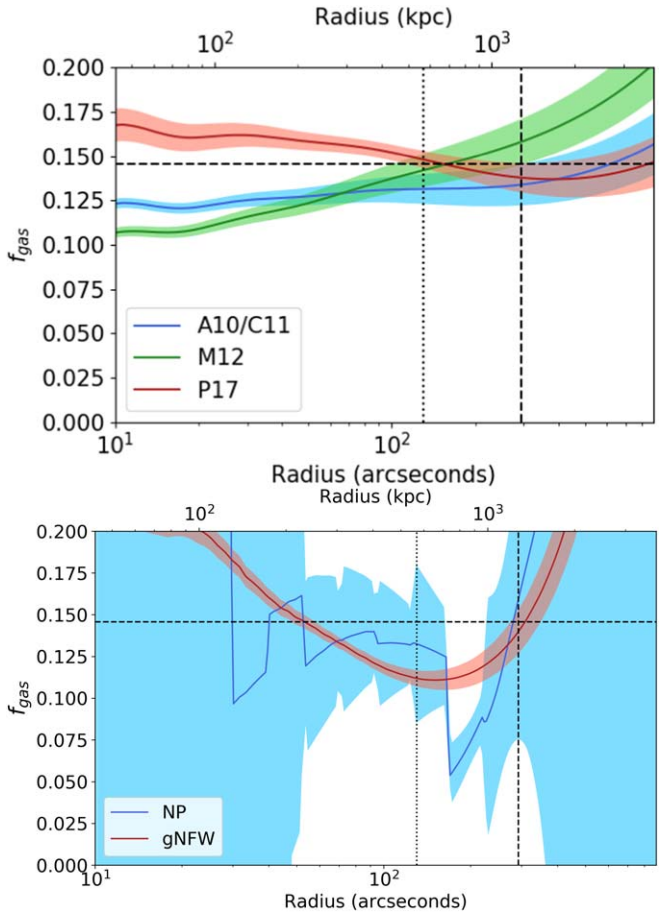

Figure 9. Upper panel: gas fractions from *Y*–*M* relations with the NP pressure profile model assuming an NFW mass profile and a constant mean molecular weight for the total mass. Bottom panel: $f_{\rm gas}$ with respect to hydrostatic masses of the NP and gNFW models for the total mass. In both panels, the vertical lines are as in Figure 4. The horizontal line is the universal cosmological baryon fraction, Ω_b/Ω_m.

be sufficiently sampled, Minkasi does not inherently limit the scales at which a model can be constrained.

We find that the A10 profile (with α, β, and γ fixed, as specified in Section 5.1) fitted to our data are in good agreement with our NP profiles. Although this is only one cluster, this acts as further indication that the A10 profile is a good descriptor of pressure profiles of galaxy clusters, especially relaxed galaxy clusters. By extension, we find that, at least for relaxed clusters, it is reasonable to fix the shape of the pressure profile to the A10 profile fit for a cluster when the data quality or angular coverage do not allow for proper NP constraints (see also Appendix C). In the case of Zwicky 3146,

the deep MUSTANG-2 observations were critical to achieving the constraints on the NP pressure profile that we found.

We have shown that it is possible to constrain the pressure profile non-parametrically beyond the FOV in SZ TODs. We found that our results are remarkably stable across a range of smoothing kernels when estimating the noise model. Furthermore, the agreement with the *XMM-Newton*-derived pressure profile reinforces our confidence in the results. However, we note that some conflicts arise in products derived from our pressure profiles, such as the hydrostatic mass bias (Section 6.3) and the entropy profiles (Section 6.4).

6.3. Mass Estimates

6.3.1. Our Mass Estimators

We have estimated the mass from our pressure profiles via three estimators: (1) *Y–M* scaling relations, (2) assuming HE in combination with X-ray determined electron densities, and (3) application of the VT assuming uniform quantities $f_{\rm gas}$ and μ_e and assuming that the matter profile follows a NFW profile. Where (2) and (3) produce mass profiles, (1) a single *Y–M* relation is defined at a specific radius. Thus, we have chosen 6 *Y–M* relations (3 at R_{500} and 3 at R_{2500}) from A10, C11, M12, and P17. Our mass estimates encompass a broad range; in particular, our minimum mass estimate is discrepant with our maximum estimate. Similar results have been found in other works (e.g., Hasselfield et al. 2013; Schrabback et al. 2018), thus reaffirming that the choice of mass estimation method (e.g., assumed *Y–M* relation) is important.

Mass estimates from our gNFW (A10) pressure profile tend to be lower than our mass estimates, at both M_{500} and M_{2500} from our NP pressure profile. At M_{500}, the gNFW masses are in agreement with the NP masses as they are within 1σ. We reiterate that the statistical errors on the gNFW masses reflect the (artificially) constrained pressure profile shape and are thus quite optimistic.

With the exception of A10 and C11, which tie their masses to hydrostatic masses, the other *Y–M* relations can trace their mass estimates to either weak lensing (M12) or numerical simulations (P17). At R_{500}, the P17 mass estimates appear consistent with the A10 (hydrostatic) mass estimates; however, M12, which comes from weak lensing, falls short of the other two *Y–M* mass estimates, as well as our HE and VT estimates. At R_{2500}, the various mass estimates tend to agree in the NP model, with the *Y–M* mass from P17 being slightly low. However, for the gNFW model, $M_{\rm HE}$ is higher than the other respective mass estimates.

Mass estimates assuming thermal HE are expected and generally found to be biased low because they do not account for non-thermal pressure support (e.g., Ettori et al. 2011). The hydrostatic mass bias is given by

$$b = \frac{M_{\rm tot} - M_{\rm HE}}{M_{\rm tot}}, \tag{17}$$

with $M_{\rm tot}$ being the (true) total mass. The bias is typically found to be between 0.1 and 0.3 (e.g., Hurier & Angulo 2018, and references therein). While Ruppin et al. (2019) find that a few (individual) clusters have negative b; these are disturbed clusters. Rather, as in Figure 6 of Ruppin et al. (2019), all of the relaxed clusters have a positive b.

It is interesting that for the gNFW pressure profile, our hydrostatic masses at R_{500} and R_{2500} are above all respective *Y–M* mass estimates. However, for our NP pressure profile, our hydrostatic masses are contained within the range of estimates from *Y–M* relations. While our hydrostatic masses are in statistical agreement, the interpretation of that from the gNFW model is not straightforward vis à vis hydrostatic mass bias. We take this to be suggestive that while the assumed gNFW pressure profile shape is close to the actual pressure profile, more freedom in the model (we had restricted α, β, and γ) could improve the agreement between the hydrostatic and *Y–M* mass estimates.

Our mass estimates from the VT, $M_{\rm VT}$, have been calculated with the same assumptions as in Mroczkowski (2011), restricting the fitted region to radii outside the central 100 kpc owing to small differences between the gNFW and NP pressure profiles in the core. Because $M_{\rm VT}$ relies on a fit over a range of radii and only has two fitted parameters, the resultant mass profile and consequently $M_{\rm VT}(R_{500})$ is determined primarily by the pressure profile bins with greatest constraints—those within R_{2500}. In contrast, the other mass estimates still have greater susceptibility to the pressure profile at large radii (where constraints are weakest). Mass estimates from *Y–M* relations are well behaved because we have restricted pressure values to be positive-definite, and Y is a cumulative value. However, the constraints on the pressure close to R_{500} are closely tied to the resultant constraints on Y_{500} and consequently M_{500}. Finally, hydrostatic mass at a single point is only informed by the derivative of the pressure profile and electron density at that point. Thus, it is susceptible to the greatest statistical noise.

In the context of Zwicky 3146, $M_{\rm VT}(r)$ continues to increase close to R_{500}. However, $M_{\rm HE}(r)$ starts to turn over around R_{500} and $Y(r)$ is increasing very little. There is not enough weight at large radii to drive $M_{\rm VT}$ closer to $M_{\rm HE}$ and the masses from *Y–M* relations.

6.3.2. Comparison of our Masses Relative to Previous Values

As before, the Minkasi pipeline pressure profiles recover well the pressure profile beyond MUSTANG-2's FOV, and moreover, they are in good agreement with the pressure profile from *XMM*. However, the various methods of mass estimation employed in this work have non-trivial scatter in an era when accuracy to better than 10% (e.g., Applegate et al. 2014; Bocquet et al. 2019; Miyatake et al. 2019) is the goal. Somewhat surprisingly, the *Y–M* relation based on weak-lensing masses (M12) appears biased low among the other mass estimators at R_{500}. One of the most recent mass estimate in the literature comes from weak lensing (Okabe & Smith 2016), and it too underestimates the mass relative to other mass estimates in the literature and those found in this work. Yet, more recently, Nagarajan et al. (2019) and Klein et al. (2019) present a weak-lensing estimate that is much closer to our mass estimates, and adopting our $M_{\rm HE}$ estimates, we find hydrostatic mass bias parameters 0.07 ± 0.16 (for our gNFW model) and 0.07 ± 0.29 (for our NP model), where we have only propagated statistical errors. As the mass estimate from Okabe & Smith (2016) and that from Klein et al. (2019) are in tension at over 3σ, this suggests that systematics have yet to be understood, notwithstanding the agreement found between the APEX–SZ and LocuSS samples (Klein et al. 2019). In the literature, weak-lensing estimates prior to Okabe & Smith (2016) have large uncertainties and thus are consistent with our

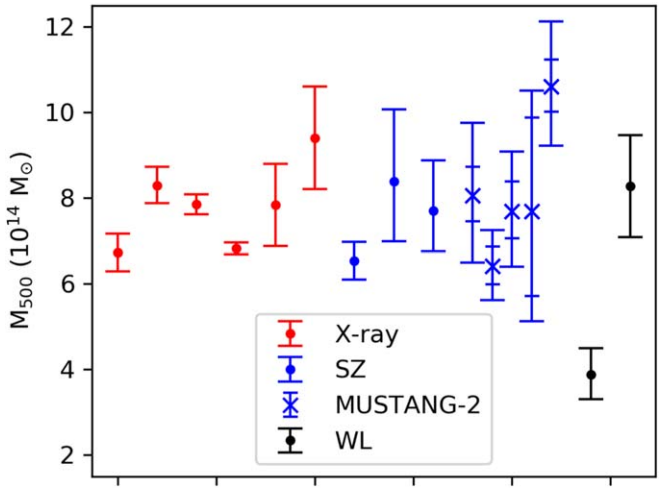

Figure 10. Estimates of M_{500} with uncertainties less than 20% from Table 1 and color-coded based on the observation type. WL stands for weak lensing. Here, extrapolated M_{500} values have their corresponding uncertainties extrapolated, if available. Some uncertainties from the literature include systematic errors while others do not; thus some caution is warranted when interpreting this plot. The MUSTANG-2 points show the mass estimates using the NP model, where the error bars show statistical uncertainties (partial error bars) and statistical plus systematic uncertainties, added linearly (full error bars).

results, and similarly do not produce tight constraints on the hydrostatic mass bias.

We present our mass estimates alongside those from the literature with uncertainties less than 20% in Figure 10, where we see broad agreement between the ICM-based masses. Of the ICM-based mass estimates, we find the minimum and maximum come from MUSTANG-2. This highlights the importance of mass estimation method. We find that all ICM-based masses appear to scatter about 8×10^{14} $M_\odot$. Of the recently derived masses from SZ, ACT and MUSTANG-2, in particular $(Y\text{–}M)_1$ in Table 2, arrive at similar mass estimates, while Planck recovers a slightly lower mass than ACT and MUSTANG-2. These three mass estimates have used the same underlying Y–M relation, and the three instruments have varying levels of detection significance. ACT detects Zwicky 3146 at 14σ, Planck at 8.4σ, and MUSTANG-2 at 61σ. We note that our extrapolated value of M_{500} from Owens Valley Radio Observatory (OVRO)/BIMA is also in agreement with ACT, Planck, and MUSTANG-2.

Given the agreement among ICM-based mass estimates and the expectation that ICM biases are minimized for relaxed clusters (e.g., Biffi et al. 2016), the discrepancy between the ICM-based masses for Zwicky 3146 and the sole well-constrained (uncertainties <20%) weak-lensing mass estimate (Okabe & Smith 2016) indicates a need for an improved understanding of our mass estimation methods and systematic uncertainties. In particular, the weak-lensing mass estimate, being less than the ICM-based mass estimates, presents a challenging interpretation.

6.4. Additional Thermodynamic Profiles

Beyond mass estimates, we use the SZ-derived pressure profiles in combination with the X-ray-derived electron density to calculate temperature profiles, entropy profiles, and gas (mass) fraction profiles. These profiles are of intrinsic interest and also serve to further check consistency.

From the temperature profile, we find that temperature begins to decrease around R_{2500}, which is slightly larger than what was found for the average temperature profile in V06. The temperature does appear to drop quite low beyond R_{500} for both our NP and gNFW models (Figure 7).

The drop in temperature at the outermost radii has a more pronounced consequence in the entropy profile. The entropy profile is expected to follow a power law outside of the core; simulations predict it will only turn over beyond R_{200}, while a handful of observations, largely of merging systems, show a turnover at and perhaps just interior to R_{200} (e.g., Walker et al. 2019). Thus, the turnover just before R_{500} appears suspect, especially as it only concerns one pressure profile bin. In Appendix B we investigate the impact on mass estimation if the entropy trend continued along its power law ($\alpha = 1.39$ for the NP model) in the event that this outermost bin is erroneously biased low in our data processing.

7. Conclusions

We have taken deep observations of Zwicky 3146 with MUSTANG-2. These observations have allowed us to produce NP constraints on the pressure profile in the radial range $5'' < r < 300''$ through a newly developed processing pipeline, dubbed Minkasi. The pressure profile recovered is in excellent agreement with the pressure profile derived from *XMM*.

Our M_{500} estimates encompass a range, where our highest mass estimate ($10.6^{+1.1+0.9}_{-1.1-0.8} \times 10^{14} M_\odot$) is inconsistent with our lowest mass estimate ($6.13^{+0.17+0.19+0.33}_{-0.17-0.19-0.32} \times 10^{14} M_\odot$). If we exclude these estimates (Y–M from M12 and $M_{\rm VT}$ for both NP and gNFW models), we find that the remaining mass estimates are in agreement, and we take our fiducial mass to be $8.06^{+0.67}_{-0.61}$ ($\pm 7.9\%$ stat) $^{+0.45}_{-0.42}$ ($\pm 5.4\%$ sys, Y–M) $^{+0.58}_{-0.54}$ ($\pm 6.9\%$ sys, cal.).

Our hydrostatic mass estimates at M_{500} are in agreement with total mass estimates from the A10 and P17 Y–M scaling relations. Interpretation of the hydrostatic mass bias is not straightforward, as the total mass is not well constrained in this analysis; namely both our M_{500} masses from P17 (simulation-based) and M12 (weak-lensing-based) fall below those from A10 (hydrostatic-based). Early weak-lensing mass estimates of Zwicky 3146 have large error bars; recent estimates (Okabe & Smith 2016; Klein et al. 2019) have quoted uncertainties less than 20%. Of those two, the estimate from Okabe & Smith (2016) falls below all of our M_{500} estimates, while that from Klein et al. (2019) falls above most of our mass estimates, and consequently is more in line with expectation. The proximity of values among $M_{\rm HE}$ and Y–M (excluding M12) mass estimates, and those from Klein et al. (2019), suggests that there is little hydrostatic mass bias (0%–10%) and consequently little non-thermal pressure support interior to R_{500} in Zwicky 3146. The fact that all our M_{500} estimates from Y–M relations fall below $M_{\rm HE}$ from the gNFW (A10) pressure profile model suggests that our restriction to A10 values of α, β, and γ was too strict.

Analysis of other thermodynamic quantities, such as the temperature profile and entropy profile, along with the hydrostatic mass profile, suggests that the pressure close to and beyond R_{500} may be underestimated. Within the NP model, we adjust the outermost pressure bin such that the entropy profile continues on a straight power law. In doing so, we find that $M_{\rm HE}$ drops by almost a factor of 2, while the Y–M masses are minimally altered. Thus, while the adjustment presents a more coherent picture with respect to the entropy profile, it

conversely disrupts the hydrostatic mass profile. In either interpretation, we have some indication of departure from HE close to R_{500}. Thus, while we cannot clearly discern that our outermost pressure profile bin is biased low, we cannot conclusively exclude this possibility. By extension, we may have an additional systematic error in our mass estimates, which we are currently unable to quantify.

Part of exploring the tensions in mass estimates will include a more thorough analysis of the physics within Zwicky 3146. In particular, we have begun a more detailed investigation into sloshing and pressure fluctuations within Zwicky 3146. These investigations aim to directly constrain the non-thermal pressure support. Beyond these additional analyses of the ICM physics, there is equally room to better understand the systematic uncertainties involved in weak-lensing mass estimates, especially concerning Zwicky 3146.

This work is supported by the NSF award no. 1615604 and by the Mt. Cuba Astronomical Foundation. S.S. is supported by NASA NSTRF NNX14AN63H. C.S. is supported in part by *Chandra* grants GO7-18122X/GO8-19106X and *XMM-Newton* grants NNX17AC69G/80NSSC18K0488. M.G. is supported by the *Lyman Spitzer Jr.* Fellowship (Princeton University) and by NASA *Chandra* grants GO7-18121X/GO8-19104X/GO9-20114X. This paper makes use of the following ALMA data: ADS/JAO.ALMA#2011.0.00001.CAL. ALMA is a partnership of ESO (representing its member states), NSF (USA), and NINS (Japan), together with NRC (Canada), *MOST* and ASIAA (Taiwan), and KASI (Republic of Korea), in cooperation with the Republic of Chile. The Joint ALMA Observatory is operated by ESO, AUI/NRAO, and NAOJ. The National Radio Astronomy Observatory is a facility of the National Science Foundation operated under cooperative agreement by Associated Universities Inc. GBT data was taken under the project ID AGBT18A_175. Basic research in radio astronomy at the Naval Research Laboratory is supported by 6.1 Base funding. The authors would like to thank Stefano Andreon and Eric Murphy for valuable input provided. The authors would also like to thank the anonymous referee for helpful comments.

Facilities: GBT, *XMM*.

Software: ds9 (Smithsonian Astrophysical Observatory 2000; Joye & Mandel 2003), Astropy (Astropy Collaboration et al. 2013; The Astropy Collaboration 2018).

Appendix A
Appendix Self-Consistency

Computing M_{500} is equivalent to finding R_{500} as $M_{500} = (4\pi/3) \times 500 \times \rho_c \times R_{500}^3$. Any self-consistent M_{500} must then lie along the curve for all possible R_{500} values (i.e., all radii); see Figure 4. For mass estimates from HE (dashed red curve) and the Virial theorem, where we have mass curves, we simply find where those mass curves cross a reference M_{500} curve (solid red line).

By extension, a reference $Y_{\rm sph}$ curve (line in log-log space) is created from the reference M_{500} curve and the selected Y–M relations, as expressed by

$$h(z)^{-2/3} Y_{\rm sph} = 10^A \times M^B, \quad (18)$$

where A is the logarithmic normalization and B is the logarithmic slope. The relations used are those found in A10, C11, M12, P17, and are tabulated in Table 4. In Figure 11, a reference $Y_{\rm sph}$ curve is the solid blue line, and the measured $Y_{\rm sph}$ is given by the dashed blue curve.

Table 4
Temperature Parameters

Relation	A	B
$(Y–M)_{\rm A10}$ (R_{500})	1.78	−30.515
$(Y–M)_{\rm M12}$ (R_{500})	2.273	−28.735
$(Y–M)_{\rm P17}$ (R_{500})	1.685	−29.073
$(Y–M)_{\rm C11}$ (R_{2500})	1.637	−28.13
$(Y–M)_{\rm M12}$ (R_{2500})	1.818	−30.669
$(Y–M)_{\rm P17}$ (R_{2500})	1.755	−29.683

Note. $Y_{\rm sph}$–M relations expressed in the form of Equation (18). The relations are taken from A10, C11, M12, P17.

We see that the hydrostatic mass curve is subject to spurious (negative) masses where the pressure increases. This is seen at small radii where the number of independent measurements is small and radio sources contribute to weaker constraints. Thus these small radii are excluded when finding where the red curves (dashed and solid) intersect. The measured $Y_{\rm sph}$ curve is an integrated quantity, and is comparatively well behaved.

Appendix B
Appendix Profile Adjustments

While we recover the pressure profile beyond the FOV very well, the very last bin appears to be biased low, as evidenced by our entropy profile (Sections 5 and 6). We thus investigate how our results change if we assume that our entropy profile should continue as a power law through the last radial bin, as had been used in the NP pressure profile. To do this, we perform two separate adjustments: first, we modify just the outermost pressure bin, and second (using the original pressure profile), we modify the corresponding electron density bin when matched to the pressure profile binning.

Figure 12 shows the adjusted pressure profile (with original electron density and original [old] pressure profile for reference) in the upper panel, and the subsequent hydrostatic mass profile (with old $M_{\rm HE}$ profile in red and $M_{500} = 4\pi\rho_c\ 500\ r^3/3$ line in black for reference). The full set of resultant (adjusted) masses are reported in Table 5. When adjusting the outermost pressure bin, we find that the new pressure value is 2.3× higher than it was originally. This corresponds to an upward shift of 2.1σ.

Indeed, the Y–M masses increase with adjustment in pressure. Yet the hydrostatic masses increase more than the Y–M masses, and thus the hydrostatic mass biases, b, are driven further negative (Table 5). The hydrostatic masses are driven exceptionally low when adjusting the electron density. Clumping, quantified by $C = \frac{\langle n_e^2 \rangle}{\langle n_e \rangle^2}$, is a potential systematic for X-ray observations and would tend to overestimate the electron density. However, given that a diminished electron density in the outer radii dramatically worsens the hydrostatic mass bias, this does not appear to be an explanation.

Figure 12 also reveals that the "old" $M_{\rm HE}$ profile shows a decreasing mass at the largest radii. In combination with the entropy profile, this is quite suggestive that our last pressure profile bin is biased low. This is not too surprising, given the lesser coverage and weaker constraints on noise at these low-k modes in the MUSTANG-2 TODs. However, as above, a naïve

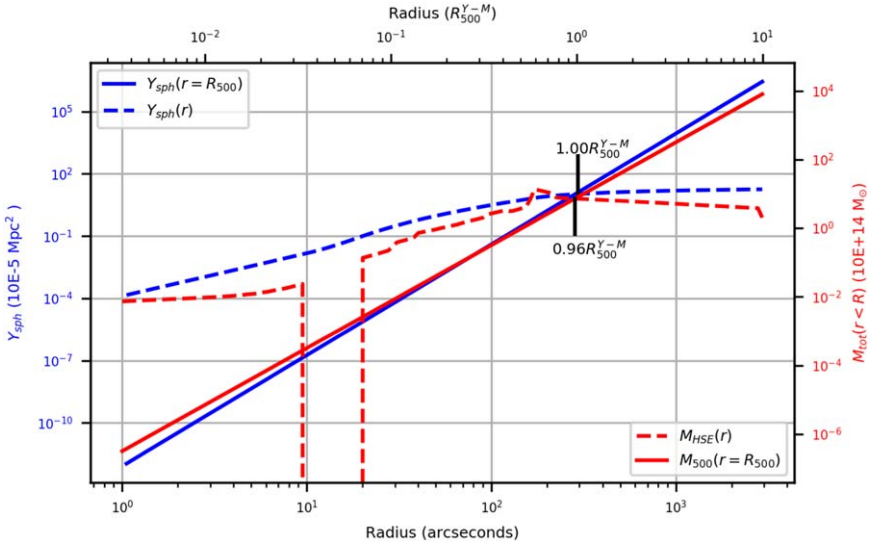

Figure 11. Hydrostatic mass is found at the point where $M_{\rm tot}(<r)$ crosses $M_{500} = \rho_c 5004\pi r^3/3$. Similarly, the self-consistent Y value is found where it crosses. Iteration is not necessary when comparing to a reference curve.

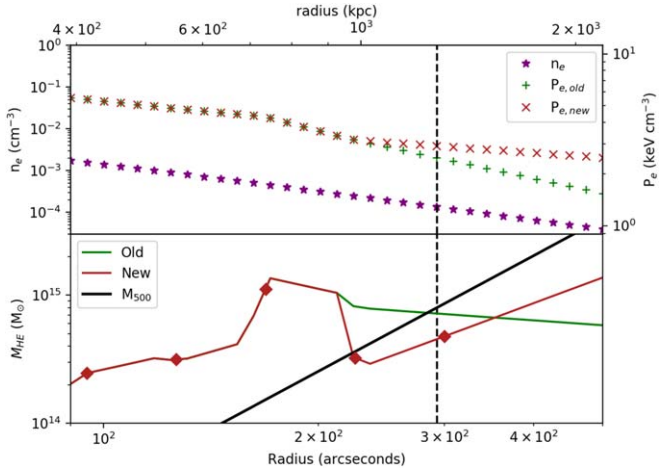

Figure 12. Using the entropy profile (Figure 8) as a guide to adjust the outermost pressure profile bin (and thus the outer slope), we obtain a new pressure profile (top panel, green X's). The bottom panel shows the old and new $M_{\rm HE}$ profiles. Note that while our pressure profiles are fitted at 12 radii (bins), we have plotted with an interpolated binning.

resolution to these symptoms results in more negative hydrostatic mass biases. That is, by extension, there is an additional problem to be solved—potentially it lies in all of the three *Y–M* relations. However, this is beyond the scope of this paper.

Appendix C
Appendix Comparing MIDAS and Minkasi

While this work has focused on the results from Minkasi data processing, we have performed much of the same analysis through our other approach, MIDAS. MIDAS benefits from its legacy of use with MUSTANG; its performance is well understood across a range of observational strategies and thus still commonly used. In light of this, a comparison of performance is prudent and follows below. For completeness, Figure 13 is a flowchart of the data reduction branches.

B.1. Data Processing with MIDAS

For each scan:

(1) A pixel mask is defined based on responsivity of detectors from instrument setup at the beginning of the run; unresponsive detectors are masked out.
(2) For each scan, the TODs are read in (2ms integrations) and averaged to larger time bins (20 ms integrations). Often, we apply a high- and low-pass filter to our TODs. The high-pass filter is chosen to filter out scales larger than the FOV (given our scanning speed). Similarly, the low-pass filter is chosen to filter out scales much smaller than our resolution. For this work, we adopted a high-pass filter at 0.08 Hz and a low-pass filter at 41 Hz.
(3) Gain and opacity corrections are applied to our data.
(4) Noise templates are constructed and fit to the data. The simplest form is to have one common mode across all detectors (typically the median). In addition to a common-mode template, a high order (∼20) order polynomial is simultaneously fit. The fits are done per detector, and subsequently the fitted templates are subtracted. Alternatively the template may be the N (N is chosen by the user; usually between 2 and 5) principal components of TODs.
(5) The cleaned TODs are checked for glitches, where a small portion of the TOD (from just before to just after each glitch) is flagged. Detector weights are assigned based on the rms of the corresponding TOD.
(6) The cleaned TODs are passed to a gridding routine. A data map and a weight map are created. For this cluster, we use 2″ pixels.

B.2. Comparing the Performance of the Two Methods of Data Processing

Within MIDAS, for Zwicky 3146 we find that low-pass filters between 0.06 and 0.09 Hz sufficiently reduce the atmospheric signal, while still retaining much of the SZ signal. Our final processing uses a low pass at 0.08 Hz. Modulation of

Table 5
Adjusted M_{500} Mass Estimates

Adjustment	Quantity	$(Y\text{–}M)_{\rm A10}$ $(10^{14}M_\odot)$	$(Y\text{–}M)_{\rm M12}$ $(10^{14}M_\odot)$	$(Y\text{–}M)_{\rm P17}$ $(10^{14}M_\odot)$	$M_{\rm HE}$ $(10^{14}M_\odot)$	$M_{\rm VT}$ $(10^{14}M_\odot)$
None	M_{500} $(10^{14}M_\odot)$	$8.06^{+0.67+0.45+0.58}_{-0.61-0.42-0.54}$	$6.41^{+0.37+0.04+0.35}_{-0.36-0.04-0.33}$	$7.69^{+0.70+0.10+0.59}_{-0.64-0.10-0.55}$	$7.69^{+2.19+0.63}_{-1.98-0.59}$	$10.6^{+1.1+0.9}_{-1.1-0.8}$
	$b_{\rm old}$	0.05	−0.20	0.0	⋯	⋯
New P_e	M_{500} $(10^{14}M_\odot)$	8.39	6.52	8.06	3.77	10.3
	$b_{\rm new}$	0.55	0.42	0.53	⋯	⋯
New n_e	M_{500} $(10^{14}M_\odot)$	8.04	6.41	7.73	12.9	10.6
	$b_{\rm new}$	−0.60	−1.01	−0.69	⋯	⋯

Note. Resultant masses when adjusting the pressure in the last bin of the NP model. As the "new" masses are not derived directly from the (true) data, the error bars are not reported. The hydrostatic mass bias, b is calculated as $(M_{Y-M} - M_{\rm HE})/M_{Y-M}$ for the respective Y–M relation. We note that $(Y\text{–}M)_{\rm A10}$ is derived from hydrostatic masses, and thus the respective value for b should be close to zero.

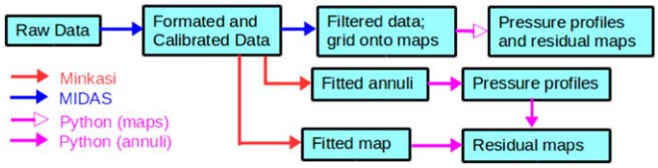

Figure 13. Flowchart for how various data products are produced.

other processing parameters has comparatively minor effects on the resultant map(s).

The recovered signal between MIDAS and Minkasi is illustrated via the transfer function (left panel) and surface brightness profile with point sources removed (right panel) in Figure 14. While the bulk of the difference in the recovered surface brightness profiles is due to the difference in transfer functions, we also note that the Minkasi surface brightness profile is deconvolved (from the MUSTANG-2 beam), while the MIDAS surface brightness profile is not. Within MIDAS, the sources are modeled as point sources with the average beam for all observing nights, taken as a single spherically symmetric Gaussian with FWHM of 10.″7.

B.3. Pressure Profile Fitting and Results

Pressure profile fitting to MIDAS maps is very similar to that in Minkasi. The same line-of-sight integration schemes are used. The major difference is that once we have calculated a Compton y profile and converted it to brightness temperature, $T_{\rm B}$, we must grid it onto our map, convolve by the MUSTANG-2 beam, and apply our transfer function (the blue curve in Figure 14). We simultaneously fit the six point sources, which also have the transfer function applied to them. Given our reduced transmission at large scales with MIDAS, we use 10 bins logarithmically spaced between 5″ and 3′ in our NP model.

The NP constraints in the MIDAS profile show a drop at our radial FOV. The two outermost points are each $\sim 2\sigma$ below the profiles recovered by Minkasi (and also *XMM*). As is found in many other ground-based single dish SZ experiments, recovery at or beyond the FOV is prone to systematic errors when TODs are processed by subtracting a common mode (or principle components). Interestingly, the MIDAS A10 profile shows a higher central pressure, which could be due to point sources degeneracies coupling to gNFW parameter degeneracies.

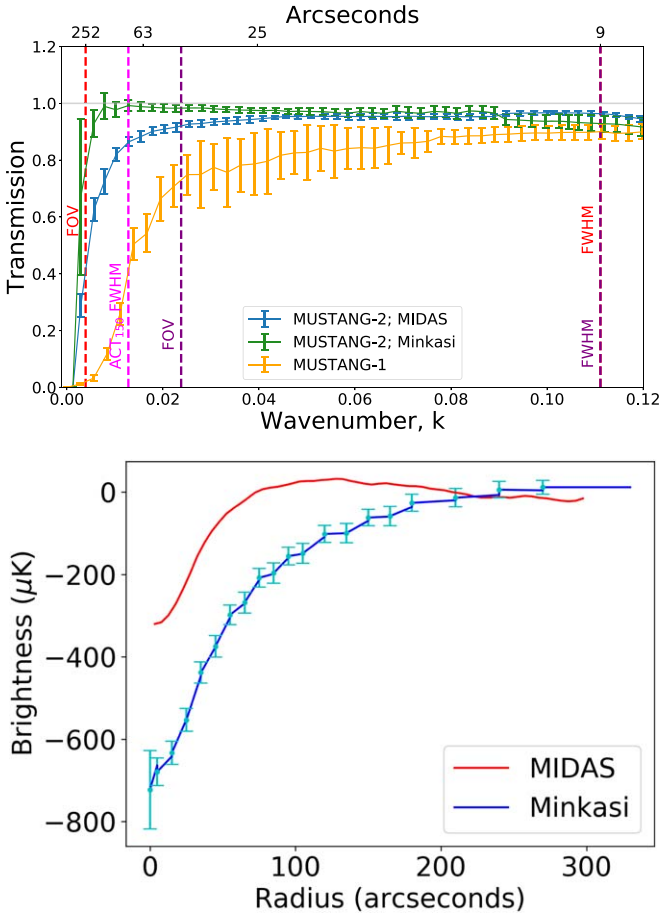

Figure 14. Top: the transfer function of MUSTANG-2 shows a marked improvement over that of MUSTANG-1. We also note the overlap with ACT (especially the band centered at 146 GHz, noted as 150 in this figure). Bottom: the surface brightness profile for Zwicky 3146 as determined by Minkasi (in concentric annuli, as plotted) and by MIDAS; the impact of the transfer function(s) is evident.

B.4. Mass Estimates

We repeat the mass estimations that were done on the Minkasi-derived pressure profiles (Sections 4.3 and 5.2 for the MIDAS branch) and tabulate the results in Table 6. Within the MIDAS branch, $M_{\rm HE}$ (both M_{2500} and M_{500}) are clearly lower than their other respective mass estimates; this is due to the poor pressure profile recovery at and beyond the radial FOV within the MIDAS branch. It is clear that the M_{500}

Table 6
MUSTANG-2 Mass Estimates from MIDAS

M_Δ	Model	$(Y–M)_1$ $(10^{14}M_\odot)$	$(Y–M)_2$ $(10^{14}M_\odot)$	$(Y–M)_3$ $(10^{14}M_\odot)$	$M_{\rm HE}$ $(10^{14}M_\odot)$	$M_{\rm VT}$ $(10^{14}M_\odot)$
M_{500}	NP	$4.66^{+0.43+0.17+0.34}_{-0.20-0.17-0.32}$	$4.25^{+0.25+0.21+0.23}_{-0.14-0.20-0.22}$	$4.35^{+0.40+0.05+0.34}_{-0.20-0.05-0.31}$	$0.90^{+0.61+2.91}_{-0.83-2.84}$	$26.1^{+18.4+2.5}_{-9.5-2.3}$
	gNFW	$7.38^{+0.15+0.39+0.54}_{-0.14-0.37-0.50}$	$6.01^{+0.09+0.22+0.33}_{-0.09-0.21-0.31}$	$7.06^{+0.15+0.09+0.55}_{-0.15-0.09-0.51}$	$5.73^{+0.26+0.19}_{-0.28-0.17}$	$7.52^{+0.14+0.56}_{-0.13-0.52}$
M_{2500}	NP	$2.95^{+0.08+0.11+0.24}_{-0.05-0.10-0.22}$	$2.64^{+0.05+0.17+0.19}_{-0.04-0.16-0.18}$	$2.38^{+0.05+0.03+0.18}_{-0.04-0.03-0.16}$	$2.94^{+0.10+0.35}_{-0.20-0.16}$	$5.56^{+1.72+0.68}_{-1.52-0.61}$
	gNFW	$3.69^{+0.06+0.15+0.30}_{-0.06-0.15-0.28}$	$3.16^{+0.04+0.08+0.22}_{-0.04-0.08-0.21}$	$2.82^{+0.04+0.03+0.21}_{-0.04-0.03-0.19}$	$4.58^{+0.17+0.13}_{-0.18-0.10}$	$3.63^{+0.05+0.31}_{-0.05-0.29}$

Note. Mass estimates from MUSTANG-2 (and electron density profiles from *XMM* for $M_{\rm HE}$). $M_{\rm VT}$ is not the virial mass, as is classically defined (with respect to $R_{\rm vir}$), but rather the mass within R_Δ using the virial theorem (Mroczkowski 2011). The error bars on the *Y–M* mass are, in order, the statistical error, systematic error from the *Y–M* relation itself, and the systematic error due to calibration uncertainty. The error bars on the other mass estimates are the statistical and systematic error due to calibration uncertainty. The *Y–M* relations for M_{500} for the subscripts 1, 2, and 3 are A10, M12, P17, respectively; for M_{2500} the relations come from C11, M12, P17, respectively.

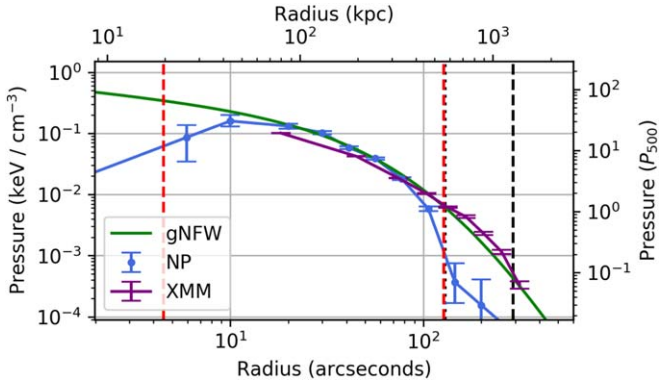

Figure 15. Pressure profiles for Zwicky 3146 as recovered by MIDAS, as well as the pressure profile as determined from *XMM-Newton*. The vertical red dashed lines are the HWHM and radial FOV for MUSTANG-2; the vertical black dashed line is R_{500} for $M_{500} = 8 \times 10^{14} M_\odot$ and the vertical black dotted line is R_{2500} for $M_{2500} = 3.5 \times 10^{14} M_\odot$.

is not physical given the M_{2500} HE. Indeed, the hydrostatic mass curve decreases beyond $\sim 120''$; thus it is not that the M_{500} is found incorrectly, vis à vis self-consistency, but this reiterates that the pressure profile is erroneously biased low at and beyond the radial FOV.

Knowing the difficulties MIDAS has recovering the pressure profile beyond MUSTANG-2's radial FOV, we additionally estimate M_{2500}, where R_{2500} lies close to the radial FOV (see Figure 15). Unfortunately, we find that the NP model recovers significantly lower masses, with the exception of $M_{\rm VT}$. However, the masses derived from the A10 pressure profile (gNFW) fits are in in good agreement with those from Minkasi. We conclude that the MIDAS processing performs equally well as Minkasi when determining pressure interior to our FOV, but that some functional fit (e.g., gNFW) should be used with MIDAS at larger radii.

Appendix D
Appendix Radio Sources in Zwicky 3146

All radio sources of concern for MUSTANG-2 are tabulated in Table 7. The six sources with 1.4 GHz data, from FIRST (Becker et al. 1994), are fit alongside some cluster model. The remaining two sources (S2 and S3) are fit in the MUSTANG-2 residual map.

Here we briefly investigate the nature of the radio sources from data available online or in the literature. A plot of the spectral energy distributions (SEDs) of the sources is found in Figure 16. For the sources with low frequency data ($\nu \leqslant 90$ GHz), we calculate (single) power laws up to 90 GHz, and find that they are good fits except for S2. We note that S2 may not be in the cluster, as Giacintucci et al. (2014) report the photometric redshift from Sloan Digital Sky Survey (SDSS) for S2 as $z_{\rm phot} = 0.34$, which would put it behind the cluster.

Sources S4 and S5 appear as a slightly extended source in MUSTANG-2. The same is true for S6 and S7. The separation is provided by FIRST; thus we follow it here. Lancaster et al. (2011) tabulate two sources which correspond to (S4, S5) and (S6, S7). That is, the OVRO/BIMA data used did not appear to sufficiently resolve these pairs of sources. We calculate a power law from the FIRST and MUSTANG-2 data and find excellent agreement with the sum of their expected flux densities at 28.5 GHz and those reported (for their respective sums) in Lancaster et al. (2011). In Table 7, we have divided the flux density the pair constituents proportional with their expected flux densities. These are also shown with circles in Figure 16.

S1, the cluster BCG, and S3 have two and three measured flux densities in publicly available Herschel SPIRE data. We obtain photometry of point sources from the level 2 maps with `photutils`[14] and incorporate the 5.5% calibration error noted in the Quick-Start Guide.[15] We do not see a peak in the BCG SED, but we do see a peak for S3.

For S3, we should thus be able to fit a modified blackbody curve:

$$I_\nu = I_0 \frac{\nu^{3+\beta}}{e^{h\nu/k_{\rm B}T} - 1}, \tag{19}$$

where I_0 is the spectral irradiance normalization, ν is the frequency, h is the Planck constant, $k_{\rm B}$ is the Boltzmann constant, T is the (redshifted) temperature of the emitting medium, and β is the modification to the standard blackbody curve due to (dust) opacity. We find $\beta = 2.7 \pm 0.4$ and $T = 7.2 \pm 1.1$, with $\chi^2 = 2.31$ and 1 degree of freedom, the probability to exceed (χ^2) due to noise alone is 0.128. This value of β is higher than perhaps expected (Draine & Lee 1984), although $\beta > 2$ has been found (e.g., Kato et al. 2018), and even $\beta > 3$ have been found (e.g., references within Shetty et al. 2009). As in Kato et al. (2018), source blending may also affect our Herschel photometry.

[14] https://photutils.readthedocs.io/en/stable/index.html
[15] https://www.cosmos.esa.int/documents/12133/1035800/QUICK-START+GUIDE+TO+HERSCHEL-SPIRE

Table 7
Zwicky 3146 Radio Sources

ID J2000	R.A. J2000	Decl. (mJy)	$S_{0.61}$ (mJy)	$S_{1.4}$ (mJy)	$S_{4.9}$ (mJy)	$S_{8.5}$ (mJy)	$S_{28.5}$[a] (mJy)	S_{90} (mJy)	S_{600} (mJy)	S_{850} (mJy)	S_{1200}
S1	$10^h23^m39\overset{s}{.}66$	$+04°11'10\overset{''}{.}8$	7.0 ± 0.4	2.04 ± 0.15	1.42 ± 0.07[b]	0.98 ± 0.03[b]	0.41 ± 0.07	0.191 ± 0.022	⋯	29 ± 5	95 ± 8
S2	$10^h23^m38\overset{s}{.}7$	$+04°11'05''$	⋯	⋯	0.31 ± 0.02[b]	0.37 ± 0.02[b]	–-	0.057 ± 0.009	⋯	⋯	⋯
S3	$10^h23^m42\overset{s}{.}3$	$+04°11'3''$	⋯	⋯	⋯	⋯	⋯	0.035 ± 0.008	34 ± 5	35 ± 5	31 ± 12
S4	$10^h23^m44\overset{s}{.}81$	$+04°10'36\overset{''}{.}7$	⋯	32.52 ± 0.15	⋯	⋯	2.83 ± 0.31[d]	0.938 ± 0.016	⋯	⋯	
S5	$10^h23^m45\overset{s}{.}26$	$+04°10'42\overset{''}{.}8$	⋯	56.69 ± 0.15	⋯	[c]41 ± 11	2.78 ± 0.31[d]	0.741 ± 0.015	⋯	⋯	⋯
S6	$10^h23^m37\overset{s}{.}51$	$+04°09'13\overset{''}{.}2$	⋯	15.06 ± 0.15	⋯	⋯	1.19 ± 0.16[d]	0.494 ± 0.019	⋯	⋯	⋯
S7	$10^h23^m36\overset{s}{.}86$	$+04°08'59\overset{''}{.}0$	⋯	12.07 ± 0.15	⋯	⋯	0.90 ± 0.16[d]	0.365 ± 0.020	⋯	⋯	⋯
S8	$10^h23^m45\overset{s}{.}27$	$+04°11'41\overset{''}{.}0$	⋯	6.06 ± 0.15	⋯	⋯	0.85 ± 0.1	0.176 ± 0.015	⋯	⋯	⋯

Notes. Radio sources in Zwicky 3146. The total (integrated) flux density for MUSTANG-2 sources is roughly 2 mJy.
[a] All 28.5 GHz flux densities transcribed here come from OVRO/BIMA (Lancaster et al. 2011).
[b] From Giacintucci et al. (2014) with VLA in C configuration.
[c] From Cooray et al. (1998); where FIRST saw two sources nearby the coordinates 10:23:45, +04:10:40, Cooray et al. (1998) categorized it as one source.
[d] Had a single value reported, corresponding to the blending (sum) of the sources in OVRO/BIMA.

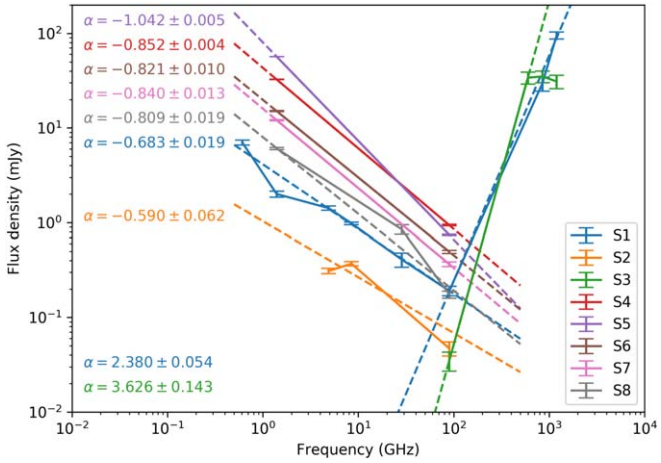

Figure 16. SEDs for all point sources tabulated in Table 7. S4, S5, S6, and S7 have interpolated/fitted points shown with circles and errors with no caps.

ORCID iDs

Charles E. Romero https://orcid.org/0000-0001-5725-0359
Jonathan Sievers https://orcid.org/0000-0001-6903-5074
Vittorio Ghirardini https://orcid.org/0000-0002-3736-8058
Simona Giacintucci https://orcid.org/0000-0002-1634-9886
Tony Mroczkowski https://orcid.org/0000-0003-3816-5372
Brian S. Mason https://orcid.org/0000-0002-8472-836X
Craig Sarazin https://orcid.org/0000-0003-0167-0981
Mark Devlin https://orcid.org/0000-0002-3169-9761
Massimo Gaspari https://orcid.org/0000-0003-2754-9258
Matthew Hilton https://orcid.org/0000-0002-8490-8117
Esra Bulbul https://orcid.org/0000-0002-7619-5399

References

Adam, R., Comis, B., Macías-Pérez, J. F., et al. 2014, A&A, 569, A66
Allen, S. W., Edge, A. C., Fabian, A. C., et al. 1992, MNRAS, 259, 67
Allen, S. W., Evrard, A. E., & Mantz, A. B. 2011, ARA&A, 49, 409
Allen, S. W., Rapetti, D. A., Schmidt, R. W., et al. 2008, MNRAS, 383, 879
Applegate, D. E., von der Linden, A., Kelly, P. L., et al. 2014, MNRAS, 439, 48
Arnaud, K. A. 1996, in ASP Conf. Ser. 101, Astronomical Data Analysis Software and Systems V, ed. G. H. Jacoby & J. Barnes (San Francisco, CA: ASP), 17
Arnaud, M., Pointecouteau, E., & Pratt, G. W. 2005, A&A, 441, 893
Arnaud, M., Pratt, G. W., Piffaretti, R., et al. 2010, A&A, 517, A92
Asplund, M., Grevesse, N., Sauval, A. J., & Scott, P. 2009, ARA&A, 47, 481
Astropy Collaboration, Robitaille, T. P., Tollerud, E. J., et al. 2013, A&A, 558, A33
Battaglia, N., Bond, J. R., Pfrommer, C., & Sievers, J. L. 2012, ApJ, 758, 74
Becker, R. H., White, R. L., & Helfand, D. J. 1994, in ASP Conf. Ser. 61, Astronomical Data Analysis Software and Systems III, ed. D. R. Crabtree, R. J. Hanisch, & J. Barnes (San Francisco, CA: ASP), 165
Bender, A. N., Kennedy, J., Ade, P. A. R., et al. 2016, MNRAS, 460, 3432
Benson, B. A., Church, S. E., Ade, P. A. R., et al. 2004, ApJ, 617, 829
Biffi, V., Borgani, S., Murante, G., et al. 2016, ApJ, 827, 112
Bleem, L. E., Stalder, B., de Haan, T., et al. 2015, ApJS, 216, 27
Bocquet, S., Dietrich, J. P., Schrabback, T., et al. 2019, ApJ, 878, 55
Bonamente, M., Joy, M., LaRoque, S. J., et al. 2008, ApJ, 675, 106
Bravi, L., Gitti, M., & Brunetti, G. 2016, MNRAS, 455, L41
Carlstrom, J. E., Holder, G. P., & Reese, E. D. 2002, ARA&A, 40, 643
Cash, W. 1979, ApJ, 228, 939
Cavagnolo, K. W., Donahue, M., Voit, G. M., & Sun, M. 2009, ApJS, 182, 12
Cavaliere, A., & Fusco-Femiano, R. 1978, A&A, 70, 677
Comis, B., de Petris, M., Conte, A., Lamagna, L., & de Gregori, S. 2011, MNRAS, 418, 1089
Cooray, A. R., Grego, L., Holzapfel, W. L., Joy, M., & Carlstrom, J. E. 1998, AJ, 115, 1388
Czakon, N. G., Sayers, J., Mantz, A., et al. 2015, ApJ, 806, 18
Dahle, H. 2006, ApJ, 653, 954
Di Mascolo, L., Churazov, E., & Mroczkowski, T. 2019, MNRAS, 487, 4037
Dicker, S. R., Ade, P. A. R., Aguirre, J., et al. 2014, Proc. SPIE, 9153, 91530J
Dicker, S. R., Korngut, P. M., Mason, B. S., et al. 2008, Proc. SPIE, 7020, 702005
Draine, B. T., & Lee, H. M. 1984, ApJ, 285, 89
Eckert, D., Ghirardini, V., Ettori, S., et al. 2019, A&A, 621, A40
Edge, A. C., Fabian, A. C., Allen, S. W., et al. 1994, MNRAS, 270, L1
Egami, E., Misselt, K. A., Rieke, G. H., et al. 2006a, ApJ, 647, 922
Egami, E., Rieke, G. H., Fadda, D., & Hines, D. C. 2006b, ApJL, 652, L21
Ettori, S., & Fabian, A. C. 1999, MNRAS, 305, 834
Ettori, S., Gastaldello, F., Leccardi, A., et al. 2010, A&A, 524, A68
Ettori, S., Gastaldello, F., Leccardi, A., et al. 2011, A&A, 526, C1
Ettori, S., Ghirardini, V., Eckert, D., et al. 2019, A&A, 621, A39
Finkbeiner, D. P., Davis, M., & Schlegel, D. J. 1999, ApJ, 524, 867
Fomalont, E., van Kempen, T., Kneissl, R., et al. 2014, Msngr, 155, 19
Foreman-Mackey, D., Hogg, D. W., Lang, D., & Goodman, J. 2013, PASP, 125, 306
Forman, W., Donnelly, H., Markevitch, M., et al. 2002, HiA, 12, 504
Foster, A. R., Ji, L., Smith, R. K., & Brickhouse, N. S. 2012, ApJ, 756, 128
Gaspari, M., Brighenti, F., & Ruszkowski, M. 2013, AN, 334, 394
Ghirardini, V., Eckert, D., Ettori, S., et al. 2019, A&A, 621, A41
Ghirardini, V., Ettori, S., Eckert, D., et al. 2018, A&A, 614, A7
Giacintucci, S., Markevitch, M., Venturi, T., et al. 2014, ApJ, 781, 9
Groener, A. M., Goldberg, D. M., & Sereno, M. 2016, MNRAS, 455, 892
Hashimoto, Y., Böhringer, H., Henry, J. P., Hasinger, G., & Szokoly, G. 2007, A&A, 467, 485
Hasselfield, M., Hilton, M., Marriage, T. A., et al. 2013, JCAP, 7, 8
Hilton, M., Hasselfield, M., Sifón, C., et al. 2018, ApJS, 235, 20
Hurier, G., & Angulo, R. E. 2018, A&A, 610, L4
Itoh, N., Kohyama, Y., & Nozawa, S. 1998, ApJ, 502, 7
Johnstone, R. M., Fabian, A. C., & Nulsen, P. E. J. 1987, MNRAS, 224, 75
Joye, W. A., & Mandel, E. 2003, in ASP Conf. Ser. 295, Astronomical Data Analysis Software and Systems XII, ed. H. E. Payne, R. I. Jedrzejewski, & R. N. Hook (San Francisco, CA: ASP), 489
Kaiser, N. 1986, MNRAS, 222, 323
Kale, R., Venturi, T., Giacintucci, S., et al. 2015, A&A, 579, A92
Kato, Y., Matsuda, Y., Iono, D., et al. 2018, PASJ, 70, L6
Kausch, W., Gitti, M., Erben, T., & Schindler, S. 2007, A&A, 471, 31
Khatri, R., & Gaspari, M. 2016, MNRAS, 463, 655
Kippenhahn, R., Weigert, A., & Weiss, A. 2012, Stellar Structure and Evolution (Berlin: Springer)
Kitayama, T., Komatsu, E., Ota, N., et al. 2004, PASJ, 56, 17
Kitayama, T., Ueda, S., Takakuwa, S., et al. 2016, PASJ, 68, 88
Klein, M., Israel, H., Nagarajan, A., et al. 2019, MNRAS, 488, 1704
Komatsu, E., Matsuo, H., Kitayama, T., et al. 2001, PASJ, 53, 57
Korngut, P. M., Dicker, S. R., Reese, E. D., et al. 2011, ApJ, 734, 10
Kravtsov, A. V., & Borgani, S. 2012, ARA&A, 50, 353
Lancaster, K., Birkinshaw, M., Gawroński, M. P., et al. 2011, MNRAS, 418, 1441
LaRoque, S. J., Bonamente, M., Carlstrom, J. E., et al. 2006, ApJ, 652, 917
Lau, E. T., Gaspari, M., Nagai, D., & Coppi, P. 2017, ApJ, 849, 54
Lau, E. T., Nagai, D., & Nelson, K. 2013, ApJ, 777, 151
Mantz, A., Allen, S. W., Ebeling, H., Rapetti, D., & Drlica-Wagner, A. 2010, MNRAS, 406, 1773
Mantz, A. B., Allen, S. W., Morris, R. G., et al. 2016, MNRAS, 463, 3582
Marrone, D. P., Smith, G. P., Okabe, N., et al. 2012, ApJ, 754, 119
Martino, R., Mazzotta, P., Bourdin, H., et al. 2014, MNRAS, 443, 2342
Mason, B., Dicker, S., Sadavoy, S., et al. 2019, arXiv:1905.05221
Mazzotta, P., Rasia, E., Moscardini, L., & Tormen, G. 2004, MNRAS, 354, 10
McCarthy, I. G., Holder, G. P., Babul, A., & Balogh, M. L. 2003, ApJ, 591, 526
McDonald, M., Gaspari, M., McNamara, B. R., & Tremblay, G. R. 2018, ApJ, 858, 45
McNamara, B. R., & Nulsen, P. E. J. 2007, ARA&A, 45, 117
Miyatake, H., Battaglia, N., Hilton, M., et al. 2019, ApJ, 875, 63
Morandi, A., Ettori, S., & Moscardini, L. 2007, MNRAS, 379, 518
Motl, P. M., Hallman, E. J., Burns, J. O., & Norman, M. L. 2005, ApJL, 623, L63
Mroczkowski, T. 2011, ApJL, 728, L35
Mroczkowski, T. 2012, ApJL, 746, L29
Mroczkowski, T., Bonamente, M., Carlstrom, J. E., et al. 2009, ApJ, 694, 1034
Mroczkowski, T., Nagai, D., Basu, K., et al. 2019, SSRv, 215, 17
Nagai, D., Kravtsov, A. V., & Vikhlinin, A. 2007, ApJ, 668, 1
Nagarajan, A., Pacaud, F., Sommer, M., et al. 2019, MNRAS, 488, 1728
Navarro, J. F., Frenk, C. S., & White, S. D. M. 1997, ApJ, 490, 493

Nelson, K., Lau, E. T., & Nagai, D. 2014a, ApJ, 792, 25
Nelson, K., Lau, E. T., Nagai, D., Rudd, D. H., & Yu, L. 2014b, ApJ, 782, 107
Nevalainen, J., Oosterbroek, T., Bonamente, M., & Colafrancesco, S. 2004, ApJ, 608, 166
Okabe, N., & Smith, G. P. 2016, MNRAS, 461, 3794
Pedersen, K., & Dahle, H. 2007, ApJ, 667, 26
Plagge, T. J., Marrone, D. P., Abdulla, Z., et al. 2013, ApJ, 770, 112
Planck Collaboration, Ade, P. A. R., Aghanim, N., et al. 2014, A&A, 571, A20
Planck Collaboration, Ade, P. A. R., Aghanim, N., et al. 2016, A&A, 594, A27
Planelles, S., Fabjan, D., Borgani, S., et al. 2017, MNRAS, 467, 3827
Pratt, G. W., Arnaud, M., Biviano, A., et al. 2019, SSRv, 215, 25
Pratt, G. W., Arnaud, M., Piffaretti, R., et al. 2010, A&A, 511, A85
Rasia, E., Tormen, G., & Moscardini, L. 2004, MNRAS, 351, 237
Romero, C., McWilliam, M., Macías-Pérez, J.-F., et al. 2018, A&A, 612, A39
Romero, C. E., Mason, B. S., Sayers, J., et al. 2015, ApJ, 807, 121
Romero, C. E., Mason, B. S., Sayers, J., et al. 2017, ApJ, 838, 86
Ruppin, F., Mayet, F., Pratt, G. W., et al. 2018, A&A, 615, A112
Ruppin, F., Sembolini, F., De Petris, M., et al. 2019, A&A, 631, A21
Salvati, L., Douspis, M., & Aghanim, N. 2018, A&A, 614, A13
Sarazin, C. L. 1988, X-ray Emission from Clusters of Galaxies (Cambridge: Cambridge Univ. Press)
Sarazin, C. L. 2003, PhPl, 10, 1992
Sayers, J., Golwala, S. R., Mantz, A. B., et al. 2016, ApJ, 832, 26
Sayers, J., Montaña, A., Mroczkowski, T., et al. 2019, ApJ, 880, 45
Schmidt, R. W., & Allen, S. W. 2007, MNRAS, 379, 209
Schrabback, T., Schirmer, M., van der Burg, R. F. J., et al. 2018, A&A, 610, A85
Sereno, M. 2015, MNRAS, 450, 3665
Shaw, L. D., Holder, G. P., & Bode, P. 2008, ApJ, 686, 206
Shetty, R., Kauffmann, J., Schnee, S., Goodman, A. A., & Ercolano, B. 2009, ApJ, 696, 2234
Shi, X., Komatsu, E., Nelson, K., & Nagai, D. 2015, MNRAS, 448, 1020
Shimizu, M., Kitayama, T., Sasaki, S., & Suto, Y. 2003, ApJ, 590, 197
Sifón, C., Menanteau, F., Hasselfield, M., et al. 2013, ApJ, 772, 25
Simionescu, A., Allen, S. W., Mantz, A., et al. 2011, Sci, 331, 1576
Smith, R. K., Brickhouse, N. S., Liedahl, D. A., & Raymond, J. C. 2001, ApJL, 556, L91
Smithsonian Astrophysical Observatory 2000, SAOImage DS9: A Utility for Displaying Astronomical Images in the X11 Window Environment, Astrophysics Source Code Library, ascl:0003.002
Snowden, S. L., Mushotzky, R. F., Kuntz, K. D., & Davis, D. S. 2008, A&A, 478, 615
Sunyaev, R. A., & Zel'dovich, Y. B. 1970, CoASP, 2, 66
Sunyaev, R. A., & Zel'dovich, Y. B. 1972, CoASP, 4, 173
The Astropy Collaboration 2018, Astropy v3.0.5: A Core Python Package for Astronomy, Zenodo, doi:10.5281/zenodo.1461536
Ueda, S., Kitayama, T., & Dotani, T. 2017, ApJ, 837, 34
van Kempen, T., Kneissl, R., & Marcelino, N. 2014, ALMA Memo 599, http://library.nrao.edu/public/memos/alma/main/memo599.pdf
Vikhlinin, A., Burenin, R. A., Ebeling, H., et al. 2009, ApJ, 692, 1033
Vikhlinin, A., Kravtsov, A., Forman, W., et al. 2006, ApJ, 640, 691
Voit, G. M. 2005, RvMP, 77, 207
Walker, S., Simionescu, A., Nagai, D., et al. 2019, SSRv, 215, 7
Walker, S. A., Fabian, A. C., Russell, H. R., & Sand ers, J. S. 2014, MNRAS, 442, 2809
Weißmann, A., Böhringer, H., Šuhada, R., & Ameglio, S. 2013, A&A, 549, A19
Wen, Z. L., & Han, J. L. 2013, MNRAS, 436, 275
Wen, Z. L., Han, J. L., & Liu, F. S. 2012, ApJS, 199, 34
White, R. L., Becker, R. H., Helfand, D. J., & Gregg, M. D. 1997, ApJ, 475, 479
Yu, L., Nelson, K., & Nagai, D. 2015, ApJ, 807, 12
Zwicky, F., Herzog, E., Wild, P., Karpowicz, M., & Kowal, C. T. 1961, Catalogue of Galaxies and of Clusters of Galaxies, Vol. 1 (Pasadena, CA: Caltech)